RESEARCH ARTICLE

Key Points:
- Simultaneous inversion methods for source and Earth conductivity are developed
- Physics-based covariances are developed to constrain source inversions
- A new 3-D model of Earth conductivity based on data from 210 sites is presented

Correspondence to:
G. D. Egbert,
egbert@coas.oregonstate.edu

Ionospheric current source modeling and global geomagnetic induction using ground geomagnetic observatory data

J. Sun[1,2], A. Kelbert[1,3], and G. D. Egbert[1]

[1]College of Earth, Ocean, and Atmospheric Sciences, Oregon State University, Corvallis, Oregon, USA, [2]Institute of Geophysics, ETH Zurich, Zurich, Switzerland, [3]USGS Geomagnetism Program, Colorado Golden, USA

Abstract Long-period global-scale electromagnetic induction studies of deep Earth conductivity are based almost exclusively on magnetovariational methods and require accurate models of external source spatial structure. We describe approaches to inverting for both the external sources and three-dimensional (3-D) conductivity variations and apply these methods to long-period ($T \geq 1.2$ days) geomagnetic observatory data. Our scheme involves three steps: (1) Observatory data from 60 years (only partly overlapping and with many large gaps) are reduced and merged into dominant spatial modes using a scheme based on frequency domain principal components. (2) Resulting modes are inverted for corresponding external source spatial structure, using a simplified conductivity model with radial variations overlain by a two-dimensional thin sheet. The source inversion is regularized using a physically based source covariance, generated through superposition of correlated tilted zonal (quasi-dipole) current loops, representing ionospheric source complexity smoothed by Earth rotation. Free parameters in the source covariance model are tuned by a leave-one-out cross-validation scheme. (3) The estimated data modes are inverted for 3-D Earth conductivity, assuming the source excitation estimated in step 2. Together, these developments constitute key components in a practical scheme for simultaneous inversion of the catalogue of historical and modern observatory data for external source spatial structure and 3-D Earth conductivity.

1. Introduction

Global geomagnetic induction studies can map electrical conductivity variations deep within the Earth, providing a view of the mantle complementary to that obtained with seismic methods [e.g., *Kelbert et al.*, 2009; *Utada et al.*, 2009; *Shimizu et al.*, 2010; *Semenov and Kuvshinov*, 2012]. At the long periods (*T*) required to image below a few hundred kilometers (i.e., *T* more than a few hours), accurate measurement of electric fields on Earth's surface becomes very challenging, and the magnetotelluric (MT) method typically becomes unreliable. At these periods magnetovariational (MV) methods—using only magnetic field components, most often obtained from geomagnetic observatories—are thus typically used. In the classic MV approach highly simplified models for external source geometry are assumed, justifying computation of local transfer functions (TFs) between field components and providing a well-defined forward problem forcing for conductivity inversion. At the longest periods (*T* > 5 days) this approach has been widely applied using so-called *C* responses, computed in the frequency domain from the ratio of the vertical and north magnetic components at a single site (Z/H) and then modeled and interpreted under the assumption of a P_1^0 geomagnetic dipole source, an idealization of the symmetric magnetospheric ring current [e.g., *Banks*, 1969; *Schultz and Larsen*, 1987; *Schultz*, 1990; *Olsen*, 1998]. A variant on this local Z/H scheme has also been applied at daily variation periods, under the assumption of a P_{m+1}^m source at daily variation periods of $T = 1/m$ day [e.g., *Bahr and Filloux*, 1989]. Nonlocal MV transfer function schemes have further been applied to deep conductivity studies, for example, the Z/Y scheme discussed in *Olsen* [1998, 1999; see also *Schmucker*, 1999a, 1999b] with local spatial gradients of the horizontal magnetic fields computed using data from multiple sites.

While these MV methods were originally developed under the assumption of a one-dimensional (radial varying) conductivity profile, with possible extensions to allow correction of the magnetic fields due to shallow conductivity anomalies [e.g., *Bahr and Filloux*, 1989; *Schmucker*, 1999b; *Kuvshinov et al.*, 2002; *Utada et al.*, 2003], they can also be applied to directly image three-dimensional conductivity variations [e.g., *Kelbert et al.*, 2008, 2009; *Shimizu et al.*, 2009; *Semenov and Kuvshinov*, 2012].

Of course, the assumption of such simple sources can only be approximately valid [e.g., see *Banks and Ainsworth*, 1992], and with the MV approach unmodeled external source might be misinterpreted in terms of

internal conductivity structure [e.g., *Püthe et al.*, 2015]. To account for contamination of the ring current fields by the auroral electrojet, *Fujii and Schultz* [2002] proposed a simple correction, based on fitting a loop of current to auroral latitude data. *Kelbert et al.* [2009] and *Semenov and Kuvshinov* [2012] applied variants on this idea to correct C responses in 3-D inversions with real data. Even with such corrections, careful data selection is typically still required, limiting data to specific period ranges, geomagnetic conditions, and/or latitude ranges. For example, in the study of *Kelbert et al.* [2009] only periods with $T > 5$ days were used, and sites with latitudes poleward of 55° geomagnetic were omitted. Even so, the possibility of contamination of the C responses by source complications could not be dismissed. *Semenov and Kuvshinov* [2012] used similar data selection criteria and expressed similar concerns about possible source complications.

As a step toward using more complex source models *Püthe and Kuvshinov* [2014] and *Püthe et al.* [2015] developed transfer function methods for sources that could be modeled as a sum of a few low-degree spherical harmonics. In these studies it was assumed that the coefficients of the source expansion could be provided as input variables for transfer function estimation, either through analysis of satellite data [*Sabaka et al.*, 2013] or by fitting fields observed in a sparse observatory array [*Püthe et al.*, 2015]. While these multivariate transfer function methods were successfully applied to recover Earth conductivity in synthetic tests (with known synthetic sources), successful application to real data has not yet been demonstrated. As we shall show subsequently, external sources cannot be modeled realistically in terms of a small number of spherical harmonics. Furthermore, there will always be some uncertainty in the external source, and any analysis should acknowledge this explicitly.

The obvious approach is to consider simultaneous estimation of the actual external source spatial structure and the Earth conductivity, through inversion of long-period geomagnetic data. Although conceptually simple and easily formulated as a mathematical problem, successful implementation of such a simultaneous inversion scheme with real data presents serious challenges. *Fainberg et al.* [1990a] outlined basic ideas, and *Singer et al.* [1993] applied these to inversion of long-period observatory data for a 1-D conductivity profile and *Dst* source fields. *Koch and Kuvshinov* [2013] develop the method further, testing joint inversion methods for 3-D conductivity and *Sq* source fields with synthetic data and simple models for 3-D conductivity. *Koch and Kuvshinov* [2015] subsequently applied these methods to real data in a continental-scale study of Australia.

Here we present a novel framework for joint source/conductivity inversion and pursue initial steps toward its successful implementation. Our approach specifically addresses two key issues. First, models for external source structure must be formulated with enough flexibility to model physically realistic complex sources while simultaneously incorporating sufficient constraints to allow well-conditioned inversion of sparsely distributed sets of ground observatories. Second, conductivity is taken to be fixed (not varying in time) and, in principle, all data, historical and modern, can help to constrain Earth conductivity. Joint inversion of all these data for temporally varying source structure would require a huge number of independent source parameters and result in a very poorly conditioned simultaneous inverse problem.

We address these issues with a scheme that can be broken into three steps. First, data are processed using a frequency domain principal component analysis (PCA), or variant, to extract spatially coherent spatial modes of the frequency domain magnetic field data. The leading PCs correspond to the dominant spatial modes of the external (magnetosphere and ionosphere) sources [*Egbert and Booker*, 1989; *Egbert*, 1989], overprinted by the corresponding induced internal fields. Compared to individual events or time windows, these modes generally exhibit the simpler, more symmetric, and larger-scale spatial structure of statistically averaged source fields. This approach also allows us to work in the frequency domain, simplifying many technical details, and provides a ready means for combining nonsimultaneous data from different eras, as discussed in *Smirnov and Egbert* [2012] and further below. This first step, which is analogous to traditional transfer function methods (but without making specific source assumptions), massively reduces the original data set, and the required number of source parameters.

The second step is to identify the actual external source structure associated with each mode. Given the generally sparse spatial distribution of observations, this source estimation will generally be nonunique and ill posed and must be tightly constrained through a priori information about physically plausible source current systems. We impose these prior constraints through a spatial covariance for external sources, developed with reference to prior knowledge of source physics and tuned to the specific period range being modeled. Given the estimates of corresponding sources, the third step is to invert for 3-D Earth conductivity structure. This can be accomplished with a 3-D global conductivity inversion scheme such as described by *Kelbert et al.*

[2008], extended to allow for general source spatial structure and to fit observed field components instead of *C* responses.

Steps 2 (estimation of the source structure) and 3 (inversion for conductivity) cannot be exactly separated and should be coupled for a truly simultaneous inversion. One simple approach [e.g., *Koch and Kuvshinov*, 2013] would be to iterate the two steps, starting with a simplified prior model for Earth conductivity, e.g., a spherically layered Earth overlain by a variable-conductance thin sheet at the surface to model oceans and continents [*Fainberg and Zinger*, 1980; *Fainberg et al.*, 1990b, 1990c; *Kuvshinov et al.*, 1999, 2007; *Sun and Egbert*, 2012a] to estimate sources. These can then be used to invert for 3-D Earth conductivity, with the resulting Earth model used to refine source estimates, etc.

Here we consider development and testing of the key components of this scheme but do not complete the task of putting these together into a true simultaneous inversion. We focus instead on development of the three steps outlined above: reducing a large heterogeneous data set to a set of magnetic field modes, modeling sources appropriate to these modes, and then using the results of the first two steps to invert for 3-D mantle conductivity variations. We summarize the approach, in a form applicable to the general problem of simultaneous source/conductivity modeling, with data processing and source modeling details focused on the case of the symmetric ring current dominated sources at periods of roughly 1–100 days. The remainder of this paper is organized as follows: In section 2 we briefly summarize a formalism for simultaneous source/conductivity inversion, establishing notation for subsequent discussions. Our approach to data processing is discussed next, in section 3, first in general terms and then specialized (and simplified) for the long-period data we consider here, where geomagnetic variations are dominated by a single mode, essentially *Dst* [*Banks and Ainsworth*, 1992; *Fujii and Schultz*, 2002]. Although close to the classical P_1^0 form at midlatitudes, there are also significant ionospheric components, particularly at auroral latitudes. Development of a covariance appropriate for these source complications is discussed in section 4. In section 5 we test our source model with a synthetic but physically realistic model of ionosphere currents, before considering regularized source inversions with observatory data in section 6. In section 7 we discuss 3-D conductivity inversion, summarizing modifications of *Kelbert et al.* [2008] required to allow for general sources and the new data types and presenting tests on synthetic data followed by application to the observatory data. Finally, we apply the inversion to the long-period observatory data using the sources estimated in section 6 and briefly compare the results to the previously published model of *Kelbert et al.* [2009].

2. Formalism for Simultaneous Source/Conductivity Inversion

The forward problem of global geomagnetic induction requires solution of Maxwell's equations, which may be symbolically described in the frequency domain ($e^{i\omega t}$) as

$$\mathbf{H} = \mathbf{G}_\sigma(\mathbf{J}), \qquad (1)$$

where **H** is the magnetic field at the surface of the Earth, **J** is the external source current density, σ is the conductivity of the Earth, and $\mathbf{G}_\sigma$ is the linear forward operator (Green's function) that maps the external current **J** to the magnetic field **H**. The magnetic fields **H** depend on both **J** (linearly) and through the Green's function on conductivity of the Earth σ (nonlinearly). Dependencies of **H**, **J**, and **G** on frequency ω are implied throughout.

In practice, all quantities are discrete. We assume the data **H** are three-component magnetic field vectors observed at N locations; i.e., a $3N$ vector $\mathbf{d}^T = [\mathbf{H}(\mathbf{r}_1), \mathbf{H}(\mathbf{r}_2), \dots, \mathbf{H}(\mathbf{r}_N)]$. The source currents **J** associated with these observations are, in general, unknown but will be represented by a linear combination of a finite set of independent components as $\bar{\mathbf{J}} = \sum_{s=1}^S c_s \mathbf{J}_s$, with S vector of unknown complex expansion coefficients $\mathbf{c} = [c_1, c_2, \dots, c_S]^T$. Definition of a concise but sufficiently rich set of source basis functions is a focus of our effort here. The Earth conductivity distribution σ is parameterized by an M vector of parameters $\bar{\sigma} = [\sigma_1, \sigma_2, \dots, \sigma_M]^T$, and the Green's function is implemented as a discrete forward solver $\bar{\mathbf{G}}_{\bar{\sigma}}$. Finally, let **L** represent evaluation of the magnetic field solutions at the observation locations, as, for example, in *Egbert and Kelbert* [2012].

Simultaneous inversion can be formulated as minimization of a penalty functional written as a sum of normalized data misfit and separate regularization terms for source and conductivity parameters; i.e.,

$$\mathcal{P}(\mathbf{c}, \bar{\sigma}) = \left(\mathbf{L}\bar{\mathbf{G}}_{\bar{\sigma}} \sum_{s=1}^{S} \mathbf{J}_s c_s - \mathbf{d} \right)^* \Sigma_d^{-1} \left(\mathbf{L}\bar{\mathbf{G}}_{\bar{\sigma}} \sum_{s=1}^{S} \mathbf{J}_s c_s - \mathbf{d} \right) + \lambda_s \mathbf{c}^* \Sigma_s^{-1} \mathbf{c} + \lambda_m \bar{\sigma}^* \Sigma_m^{-1} \bar{\sigma} . \tag{2}$$

Note that in (2) the source ($\mathbf{c}$) and conductivity ($\bar{\sigma}$) parameters are implicitly assumed to be uncorrelated, with parameters λ_s and λ_m defining the weighting of these terms relative to the data misfit. Σ_d, Σ_s, and Σ_m are predefined data, source, and conductivity (model) covariance matrices, respectively, and the superscript asterisk denotes complex conjugate transpose. In general, data for multiple periods, as well as multiple events (or spatial modes; see section 3), may be included, and the data misfit and source regularization terms in (2) will then be sums over these data components. In contrast, a single-conductivity parameter vector will always be relevant to all observations, effectively coupling the joint inverse problem over periods/events.

In this paper we focus first on the simpler problem of estimation of source parameters, with the conductivity parameter vector $\bar{\sigma}$ assumed known. In this case the discrete version of (1) can be given by the linear matrix equation

$$\mathbf{d} = \mathbf{X}_{\bar{\sigma}} \mathbf{c} , \tag{3}$$

where the sth column of the $3N \times S$ system matrix $\mathbf{X}_{\bar{\sigma}}$ gives the three components of the magnetic fields from the sth source component $\mathbf{J}_s$ sampled at the observatory locations $\mathbf{r}_i$, $i = 1, \ldots, N$, i.e., $\mathbf{L}\bar{\mathbf{G}}_{\bar{\sigma}}(\mathbf{J}_s)$. The penalty functional for this linear inverse problem then reduces to

$$\mathcal{P}(\mathbf{c}) = \left[\mathbf{X}_{\bar{\sigma}} \mathbf{c} - \mathbf{d} \right]^* \Sigma_d^{-1} \left[\mathbf{X}_{\bar{\sigma}} \mathbf{c} - \mathbf{d} \right] + \lambda_s \mathbf{c}^* \Sigma_s^{-1} \mathbf{c}. \tag{4}$$

Note that we are assuming that sources are uncorrelated between periods/modes, so the minimization of (2) decouples into a series of smaller problems, and (4) can be minimized separately for each period/mode.

Here we make the further simplification that the conductivity can be initially described with a 1-D radial profile, overlain by a thin sheet, implementing $\mathbf{G}_{\bar{\sigma}}$ following *Sun and Egbert* [2012a]. In section 7 we further discuss inversion for a general 3-D conductivity distribution, now with sources fixed. Specifically, we minimize

$$\mathcal{P}(\bar{\sigma}) = \left[\mathbf{L}\bar{\mathbf{G}}_{(\bar{\sigma})} \bar{\mathbf{J}} - \mathbf{d} \right]^* \Sigma_d^{-1} \left[\mathbf{L}\bar{\mathbf{G}}_{(\bar{\sigma})} \bar{\mathbf{J}} - \mathbf{d} \right] + \lambda_m \bar{\sigma}^* \Sigma_m^{-1} \bar{\sigma} , \tag{5}$$

where now $\bar{\mathbf{J}}$ is fixed (determined from the source estimation step). This inverse problem implicitly includes (and couples) data for all periods/events. While the solution to this problem is rather complex and involves a nonlinear inversion with iterative forward and sensitivity computations, the bulk of this approach has been previously published [e.g., *Kelbert et al.*, 2008] and requires only moderate extensions to be applied as part of our scheme.

The two minimization steps (4) and (5) may be iterated, as in *Koch and Kuvshinov* [2013], with the full 3-D Green's function used to compute the columns of the design matrix $\mathbf{X}_{\bar{\sigma}}$ in (4) for all source inversion steps past the first, but we do not consider this (nontrivial) extension further here.

3. Estimation of Frequency Domain Spatial Modes From Geomagnetic Observatory Data

Our data processing scheme is conceptually based on the frequency domain principal component analysis (PCA) originally applied to geomagnetic array data by *Egbert and Booker* [1989; see also *Egbert*, 1989, 1997, 2002]. We review the general approach as a key component of our simultaneous source/conductivity modeling scheme and then describe the simplified approach we have used for the long-period variations that we focus on in this paper. Briefly, windowed Fourier transform of three-component magnetic field time series observed at N sites results in time sequences $\mathbf{Y}_i$ of complex data vectors of dimension $3N$ for each frequency band, where i indicates segment (time window) number. These vectors can typically be approximated well as a linear combination of a small number K of spatial modes $\mathbf{U}_k$, with temporal coefficients b_{ki} characterizing variations of source structure over segments. Mathematically,

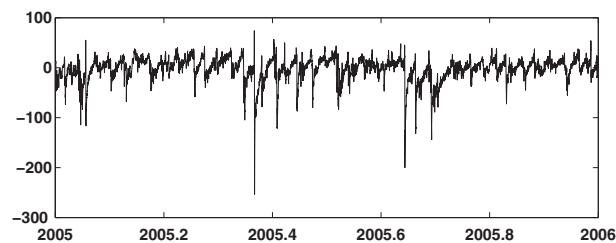$$\mathbf{Y}_i = \sum_{k=1}^{K} \mathbf{U}_k b_{ki} + \epsilon_i, \tag{6}$$

Figure 1. Estimated reference signal $R(t)$ for 1 year (2005).

where ϵ_i represents noise and unmodeled source components for time window i.

As argued in *Egbert* [1989], linearity of Maxwell's equations implies that components of the spatial modes give total (external plus induced internal) magnetic fields at the observing sites corresponding to the statistically dominant, but formally unknown, external current patterns that excite the total field variations observed by the array. The leading modes tend to be larger scale and exhibit greater symmetry, compared to actual sources associated with individual time segments. PCA thus provides a powerful means to reduce large data sets, distilling a potentially large number of possibly noisy frequency domain data vectors $\mathbf{Y}_i$ into a few well-constrained "spatial modes," which we can then use as input data for a simultaneous source/conductivity inversion. Note that the individual components of the $3N$ vectors $\mathbf{Y}_i$ correspond to the three components of the modal magnetic fields, sampled at the N sites. Not only are the dominant spatial modes a priori likely to correspond to simpler and larger-scale (and hence easier to model) sources but they also average data from many time segments, providing improved signal-to-noise ratio. The PCA approach thus offers many of the advantages of transfer functions (TFs), without requiring specific source assumptions.

Egbert [1997] and *Smirnov and Egbert* [2012] developed an extension of the standard PCA estimation scheme (which is generally based on eigenvectors of the $3N \times 3N$ spectral density, or cross-product matrix), to incorporate robust statistical estimation methods and allow for even large blocks of missing data. This extension, which further emulates the TF approach by allowing data from different eras to be combined into estimates of the spatial modes sampled at a larger number of locations, forms the basis of the approach used here. Missing data are accommodated using an iterative "crisscross" regression scheme, which alternately estimates the spatial modes $\mathbf{U}_k$ and the temporal coefficients b_{ki} of equation (6) using robust methods. This iterative scheme requires some sort of initialization, e.g., starting from an estimate of the spatial modes $\mathbf{U}_k$ obtained through conventional PCA of a "core array" (with no missing data), or by using prior knowledge of approximate source structure. We used a variant on the latter approach for this study.

Specifically, based on the well-established dominance of the symmetric magnetospheric ring current source for periods beyond a few days, we assume a priori a single spatial mode $\mathbf{U}_1$, corresponding to a source with total horizontal magnetic fields that can be approximated well at midlatitudes as a zonal dipole. Within the context of equation (6), the single spatial mode is thus initialized so that the horizontal field components correspond to a dipole structure, with geomagnetic north components varying as $\sin(\theta_g)$, where θ_g is geomagnetic colatitude. The temporal mode coefficients b_{1i} can then be estimated by solving a series of small least squares problems, one for each time segment i (i.e., minimizing misfit of equation (6) over components of $\mathbf{Y}_i$, with $K = 1$ and $\mathbf{U}_1$ taken as fixed). Only components of the data vectors $\mathbf{Y}_i$ likely to be consistent with the assumed source structure (midlatitude observatories and horizontal field components) are used in this step. With the temporal coefficients determined, robust regression methods can then be used to refine estimates of components of the spatial mode $\mathbf{U}_1$, now including all vector components at all available observatories (i.e., all latitudes). In principle this scheme can be iterated, using the new estimates of $\mathbf{U}_1$ to further refine estimates of the temporal coefficients b_{1i}, and so on, as described in *Smirnov and Egbert* [2012].

Because the reference source field spatial structure for the ring current is independent of period, the multistep PCA analysis can be slightly simplified by doing the first step in the time domain, i.e., by directly fitting hourly mean values of the geomagnetic north component of midlatitude observatories to $\sin(\theta_g)$. This results in a continuous (no gaps) time series $R(t)$ corresponding to midlatitude zonal dipole variations, quite analogous to the *Dst* index; see Figure 1 for a plot of a 1 year time segment. This reference time series can then be used as the input or predicting variable in a standard univariate TF analysis, conducted separately for each of the three components at each observatory. More specifically, we use a windowed Fourier transform, applied to $R(t)$,
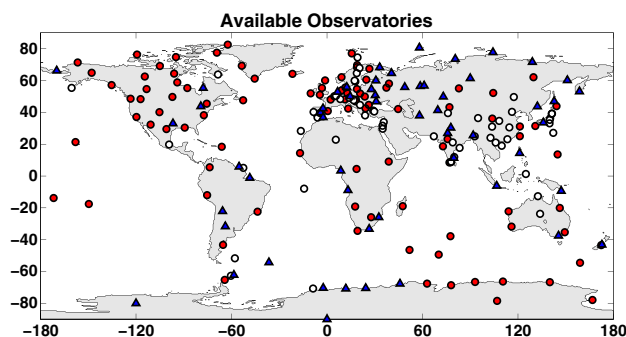
Figure 2. Full set of 220 observatories analyzed. Blue triangles indicate sites where only historical (1958–1994) data were available; white circles indicate sites with only modern (1995–2010) data, and red circles denote sites with significant amounts of data from both epochs.

to produce the coefficients b_{1i} in (6), and to magnetic field component (B_x, B_y, B_z) time series for all observatories, to produce the vectors $\mathbf{Y}_i$ (for a series of periods). Then, each of the $3N$ components of the spatial mode $\mathbf{U}_1$ is estimated using the regression M estimate, as in *Egbert and Booker* [1986]. Note that with this approach each site and field component is estimated independently, so all available data can easily be used in the estimates. Again, this scheme could be iterated, successively refining estimates of the frequency domain temporal coefficients b_{1i} and spatial mode $\mathbf{U}_1$, but we have only done a single step for the results shown below. The single spatial mode $\mathbf{U}_1$ obtained by this process represents the three components of the magnetic field at all available observatories that are coherent with the estimated (midlatitude) ring current source variations, providing suitable frequency domain field component data for the source inversion scheme outlined in section 2. Error bars for the robust estimates are obtained with the standard asymptotic approach [*Huber*, 1981] (see also *Eisel and Egbert* [2001] for a closely related application to MT impedance estimation). These error bars can be used to define a simple diagonal data error covariance for the inversions (i.e., Σ_d in (4) and (5)).

We applied this scheme to a large set of modern and historical observatory data, at a total of 220 sites (Figure 2), covering the time period 1958–2010. For modern observatories minute values (obtained from INTERMAGNET (www.intermagnet.org) and other sources) were averaged to hourly means; for older data hourly means archived at the National Geophysical Data Center (NGDC) were used. To estimate $R(t)$, only observatories at geomagnetic midlatitude (between 10 and 50°), and with a minimum of 10 years of good data were used. Both standard least squares and robust fitting schemes were tried for this step, with little discernible difference in the fitted reference signal $R(t)$. Robust regression methods improved the subsequent estimates of components of the spatial mode $\mathbf{U}_1$. As one check on consistency, data were processed in two separate time windows 1958–1994 (all from NGDC) and 1995–2010 (mostly INTERMAGNET), as well as for the full time window. Of the 111 observatories with a minimum of 5 years of data in both windows, estimates differed significantly at only three sites: Sheshan, China (SSH); Yakutsk, Russia (YAK); and Vassouras, Brazil (VSS). In all three cases results from one of the time windows appeared more reasonable (smooth variation with frequency, similar to other observatories at similar latitude), and these were selected for further analysis. For a few additional sites, using only modern data resulted in improved overall estimates; in these cases the analysis was restricted to the modern data. For all other sites all available data were used.

Estimated horizontal field vectors for the full data set are shown for a period of 18 days in Figure 3, showing the general consistency of fields with the expected P_1^0 form, particularly at midlatitudes. Deviations from this idealized form are evident at high latitudes. This is seen more clearly in Figure 4, where we plot geomagnetic north (B_x), east (B_y), and vertical (B_z) components (with 1 sigma error bars) versus geomagnetic latitude for 5 of the 13 logarithmically spaced periods (ranging from 1.2 to 100 days) used for the source and conductivity inversions described in the remaining sections. The plots of Figure 4 reveal significant and spatially coherent deviations above about 50° latitude in all components, as well as some evidence for possible complications near the magnetic equator. Note that these data are also plotted for comparison to fitted source fields in Figures 10 and 11.

Error bars in Figure 4 are generally small but increase at longer periods, where time series for some sites become short. Estimates at least a few points might be considered suspect in these plots. During the inversion steps data from a few observatories were found to be anomalous (perhaps due to time base errors), were
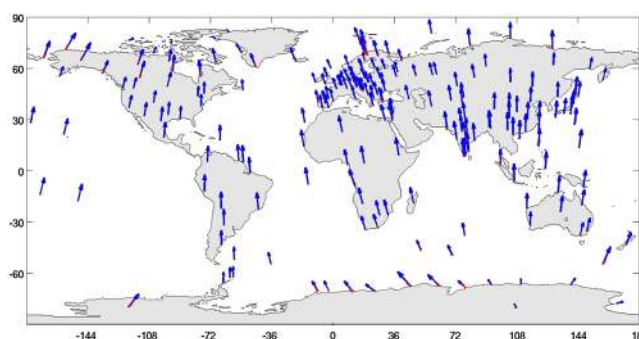
Figure 3. Plot of horizontal components of the single estimated data mode **U** derived from magnetic field components coherent with the estimated midlatitude $R(t)$ signal, at a period of $T = 18.3$ days, including all 220 observatories. Blue arrows are in-phase components; smaller red arrows are quadrature (i.e., imaginary) components. Note that vectors are mostly in phase at middle to low latitudes.

too noisy to be fit well, or were too close to a nearby site to be resolved by either the source or conductivity inversion grids. These observatories were ultimately eliminated, resulting in a total of 210 sites used for the inversions described below.

4. Source Parameterization and Covariance

As Figures 3 and 4 show, magnetic fields estimated following the previous section are dominated by a zonal geomagnetic dipole term (i.e., the classical ring current), with complications primarily at auroral and equatorial latitudes. These additional sources are also mostly zonal, as would be expected at such long periods due to rotation of the Earth: current systems in the ionosphere and magnetosphere are mostly stationary in a Sun-fixed frame, and any nonzonal structure would map to more rapid ($T < 1$ day) variations in the Earth frame relevant to the induction problem. Such geometric considerations provide important constraints on source geometry and can guide model parameterization. For example, *Schmucker* [1999a] shows that solar quiet day fields (*Sq*) can be modeled well with the first six time harmonics of the fundamental daily variation period. Due to effects of Earth rotation beneath relatively fixed sources, the spatial structure of time harmonic $p (= 1, \ldots, 6)$ is dominated by spherical harmonic degree $m = p$ and order $l = p + 1$. *Sq* source models can be improved by including a small number of nearby degrees and orders. *Koch and Kuvshinov* [2013] used $m = p-1, p, p+1$ and $l = p+1, \ldots, p+4$ in their global joint inversion studies with synthetic data, and *Koch and Kuvshinov* [2015] took a similar approach in studies with real data from a regional-scale array in Australia. While this approach may be suitable for modeling quiet day *Sq* fields (particularly over a limited domain, as in *Koch and Kuvshinov* [2015]), no similar small set of simple and natural basis functions is appropriate for modeling of long-period ionosphere sources at global scale. A principal objective here is to develop physically appropriate basis functions that can model the narrow quasi-zonal ionospheric current sources that contaminate the simpler, dominantly P_1^0, long-period magnetospheric sources. To do this, we first develop a model of random current sources. An eigenvector decomposition of the corresponding covariance of these sources then leads to a relatively small number of source basis functions $\mathbf{J}_s$ (see section 2), along with a diagonal covariance matrix Σ_s which defines the regularization of the inversion, as in (2) or (4).

Two simple physical considerations guide our development of the source model. First, for geomagnetic field variations observed at ground level, the actual 3-D external source current systems may be represented by a 2-D divergence-free toroidal equivalent current sheet flowing on a sphere of fixed height above the surface [e.g., *Sun and Egbert*, 2012b]. Second, under the influence of the Earth's main field through the Lorentz force, thermal convection driven ionospheric currents tend to flow in the direction perpendicular to the main field. It is thus advantageous to model the equivalent ionospheric current sheet using quasi-dipole (QD) coordinates [*Richmond*, 1995; *Emmert et al.*, 2010]. In this coordinate system meridians roughly follow the projection of Earth's main field lines, while latitude lines are perpendicular. QD coordinates thus allow complexity in ionospheric current systems resulting from the near-Earth nondipole magnetic field to be modeled with fewer free parameters [e.g., *Sabaka et al.*, 2004].

Based on these considerations, our model allows first for the P_1^0 source term (to model distant magnetospheric sources), with deviations from this simple form modeled as a weighted sum of three uncorrelated
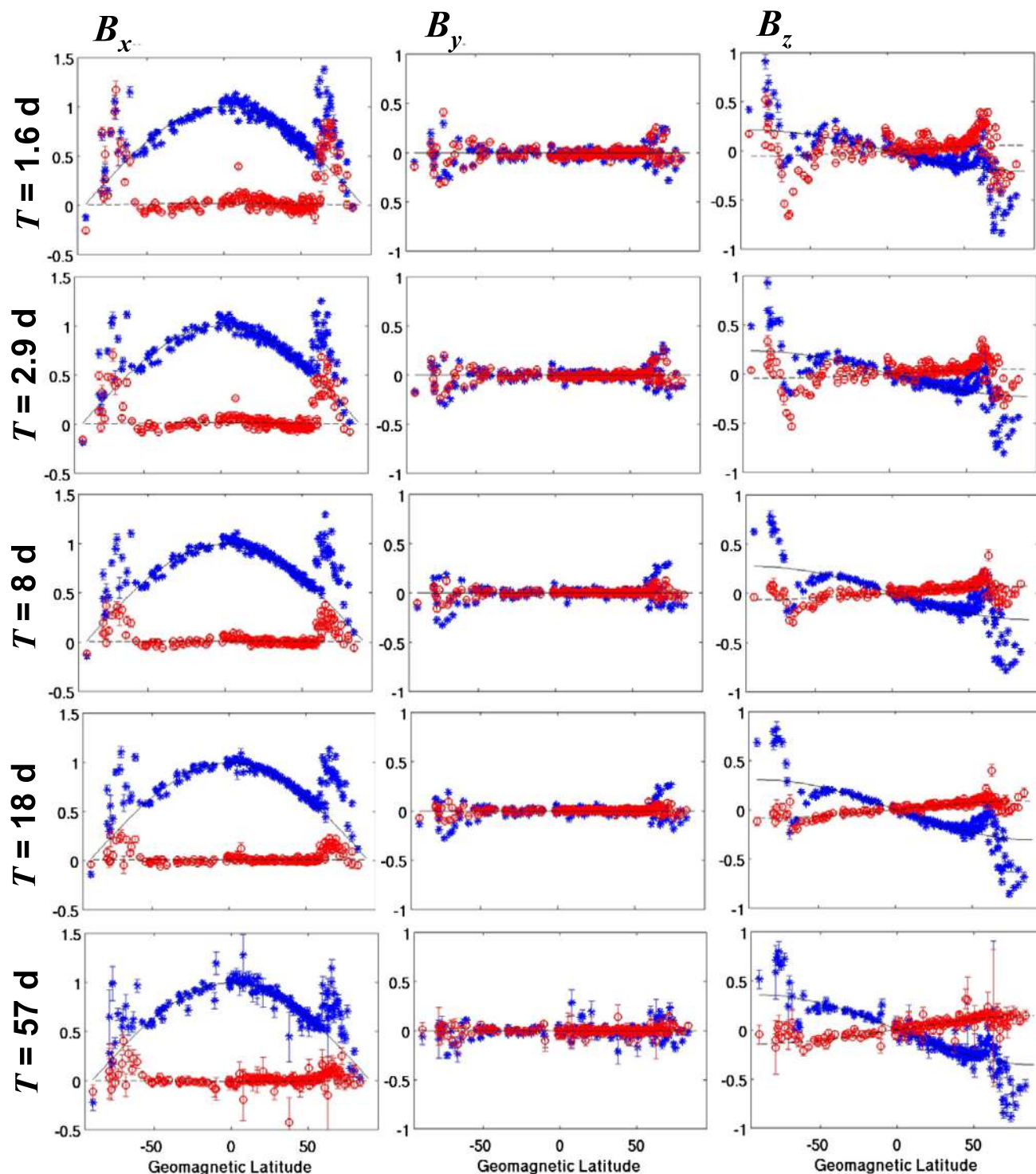
Figure 4. Plot of data modes for 5 of the 13 period bands, with real (blue) and imaginary (red) parts of the complex field components (geomagnetic coordinates) versus geomagnetic latitude. Best fitting (for midlatitudes) curves consistent with a zonal dipole source (i.e., in terms of geomagnetic colatitude θ_g, $\sin(\theta_g)$ for B_x, $\cos(\theta_g)$ for B_z, and 0 for B_y) are shown as black lines.
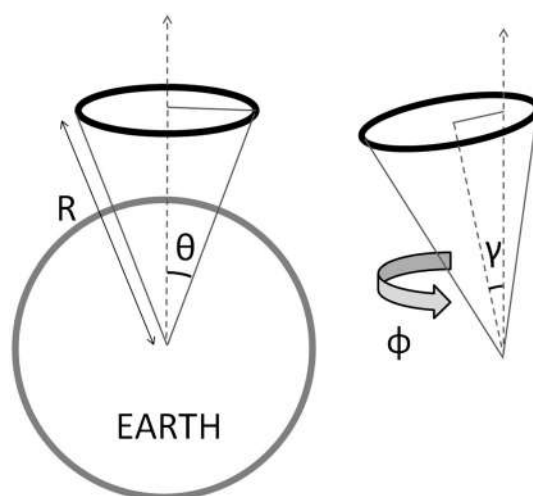
Figure 5. A single current loop is located at a fixed altitude from the surface of the Earth. Variables (θ, γ, ϕ) define the loop colatitude, its tilt from the dipole axis, and rotation angle, respectively.

quasi-zonal (in QD coordinates) current systems, corresponding to low-latitude (equatorial) as well as northern and southern auroral iono-spheric currents. Each current system consists of a number of quasi-zonal loops within the spherical current sheet. Amplitudes and correlations among these loops are latitude dependent, tuned to match the general character of the estimated data modes of section 3. The need for auroral current systems is clear, as large deviations from the classic dipole form are clearly evident at high latitudes in Figure 4. We have included a broader current system centered on the equator to allow for any deviations from a pure dipole at lower latitudes. While one might expect ionospheric current systems (which are generally organized in a Sun-fixed frame) to be averaged to zero by Earth rotation at longer periods, it is unclear that this averaging must be exact, particularly for periods of 1 – 5 days. As we shall see, the amplitude of this low- to middle-latitude current system is small (but nonnegligible) in the fitted models, especially as the period approaches 1 day.

We have selected 200 km for the altitude of the three current systems, bearing in mind that an equivalent current sheet can be situated at *any* altitude above the Earth's surface [*Sun and Egbert*, 2012b]. This is above the height of mean ionospheric currents (closer to 100 km) resulting in smoothing of source fields at the surface of the Earth. This smoothing is reasonable given that the fundamental loops are artificially narrow line currents and that the data modes represent statistically averaged source fields, which are expected to be even smoother than individual instances of the source fields. For each of the three current systems, individual current loops are generated along lines of constant QD colatitude on this surface and then tilted to varying degrees. In particular, each loop is defined by three angles $L = (\theta, \gamma, \phi)$, where θ is the nominal colatitude of the loop, γ is the tilt, and ϕ gives the rotation in longitude, as illustrated in Figure 5. A typical realization of the random current system is viewed as generated by a large collection of loops, with random parameters. We generate the covariance for this random spatial process with a systematic sampling of a large number of
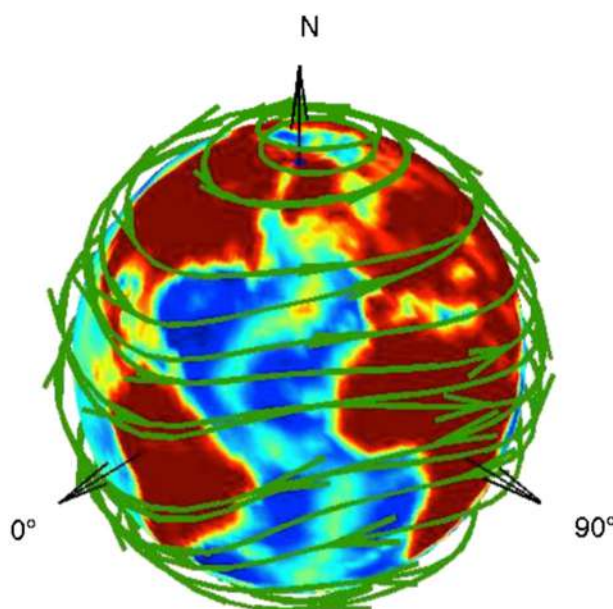

Figure 6. A collection of quasi-zonal current loops following quasi-dipole latitudinal lines.

such loops, with $\theta \in (\theta_{min}, \theta_{max})$, $\gamma \in [0, \gamma_{max}(\theta))$, and $\phi \in [0, 360°)$, all evenly distributed over the specified ranges, using a spatial resolution of 3°, sufficient to cover the Earth uniformly without discretization artifacts. Note that the maximal tilt angle is a function of θ. More specifically,

$$\gamma_{max}(\theta) = \begin{cases} \left[\theta/90°\right]\gamma_0, & \text{if } \theta \leq 90°, \\ \left[(180° - \theta)/90°\right]\gamma_0, & \text{if } \theta > 90°, \end{cases} \tag{7}$$

i.e., γ is allowed to be larger at lower latitude, to provide a relatively even loop tilt allowing for the curvature of the spherical surface. The maximal tilt angle at the equator is γ_0. A few samples of these fundamental current loops are shown in Figure 6.

The amplitude of a loop $L = (\theta, \phi, \gamma)$ is specified as a function of latitude $\tilde{\theta} = 90 - \theta$ through the formula

$$\sigma_L(L) = \cos\left(\frac{\tilde{\theta} - \frac{\tilde{\theta}_{min} + \tilde{\theta}_{max}}{2}}{\frac{\tilde{\theta}_{max} - \tilde{\theta}_{min}}{2}} \times 90°\right)^2 \cos\gamma^2 . \tag{8}$$

Thus, the assumed current variance reaches a maximum at the center latitude $\frac{\tilde{\theta}_{min} + \tilde{\theta}_{max}}{2}$ and tapers to zero at the latitude boundaries of the current system, $\tilde{\theta}_{min}$ and $\tilde{\theta}_{max}$. The variance is further modulated by the tilt angle by the factor $\cos\gamma^2$, which is maximal at 0°, and tapers to zero at 90°. These settings give most weight to strictly zonal loops that are centrally located, avoid abrupt changes in the latitudinal distribution of currents, and allow a controlled relaxation from a strictly zonal distribution to a quasi-zonal distribution, as model parameters are varied. The correlation between a pair of current loops L_1 and L_2 is specified as

$$\rho_L(L_1, L_2) = O(L_1, L_2)^\alpha , \tag{9}$$

where $O(L_1, L_2)$ is a proximity function measuring the distance between two loops (see Appendix A for details) and α is the incoherence parameter controlling how rapidly correlation between two loops falls off, with large α corresponding to more rapid decorrelation. The (L_1, L_2) element of the loops' covariance matrix is thus given by

$$\Sigma_L(L_1, L_2) = \sigma_L(L_1)\sigma_L(L_2)\rho_L(L_1, L_2). \tag{10}$$

Although the current loops provide a simple physical representation of ionospheric sources, subsequent computations are simplified if these are converted into a spherical harmonic (SH) representation, following equations (11) and (39) of *Sun and Egbert* [2012b]. We choose a maximal SH degree $l_{max} = 40$. To reduce high-frequency components caused by the nonphysical "thin wire" current loops, we thus apply a raised-cosine filter

$$f(l) = \cos\left(\frac{l}{l_{max}}\right)^2 , \tag{11}$$

where l is the SH degree, to the SH representation of the current loops. Results for all loops are stored in an $N_S \times N_L$ matrix $\hat{S}$, where N_S is the total number of SH coefficients retained for each loop and N_L is the total number of loops in the collection. For $l_{max} = 40$ in our application, $N_S = 1680$. For the spacing of loops at 3°, N_L is an order of magnitude larger. The corresponding covariance matrix for the SH coefficients is given by

$$\Sigma_S = \hat{S}\Sigma_L\hat{S}^*. \tag{12}$$

This SH covariance matrix Σ_S is symmetric but not guaranteed positive-definite. However, a truncated eigenvalue decomposition at a numerical threshold, e.g., 10^{-6}, eliminates small negative eigenvalues and further reduces effective degrees of freedom (DOF) in the source model. A truncated SH covariance is constructed for each of the three uncorrelated current systems, with the full source covariance then given by a weighted sum. The result is then normalized to have Frobenius norm one, with the overall scale in the source regularization term absorbed into the trade-off parameter λ_s in (4).

To summarize, the covariance is generated in several steps. First, current loops are generated sampling the range of colatitudes and tilts. Next, the loop covariance Σ_L is computed following (10). Finally, the covariance is converted into a covariance of SH coefficients via (12). This covariance can be further reduced using an eigenvalue decomposition, effectively representing the covariance in terms of an even smaller number of

basis functions. The parameters that must be set to completely define the covariance for a single current system are $(\theta_{min}, \theta_{max}, \gamma_0, \alpha)$, where the first three parameters control loop geometry, and the last controls the level of coherence between pairs. These parameters may in principle be different for each of the three current systems, but we assume (statistical) symmetry between northern and southern auroral currents and only distinguish between high- and low-latitude parameters. Relative amplitudes for the three current systems are similarly reduced to a single parameter, the ratio between auroral and low-latitude amplitudes, with the sum of the three weights constrained to one. Some other parameters, such as the current loops' spatial resolution at 3° and altitude at 200 km and truncation level of the SH coefficients at $l_{max} = 40$, have less material effect in the patterns of the generated current systems. After some initial tests they have been chosen at "reasonable" levels and hard coded into our implementation.

5. Source Inversion Using Independent Synthetic Data

To validate the source model described in section 4, we first consider tests with synthetic data, where we can verify the accuracy of source currents recovered by the inversion. Because our goal is to demonstrate that the proposed covariance can be used to map physically realistic sources from sparse ground sampling, we generate the synthetic current systems with a completely independent physics-based model, the thermosphere-ionosphere-mesosphere electrodynamics general circulation model (TIME-GCM) [*Richmond et al.*, 1992; *Qian et al.*, 2014]. TIME-GCM is a self-consistent model that accounts for all of the important aeronomical, dynamical, and electrodynamical processes in the ionospheric dynamo. For our tests we used a 29 day run of this model for the month of June 2002 (A. Richmond and A. Maute, personal communication, 2009). Magnetic fields, sampled once per hour on a uniform grid on Earth's surface, were transformed to the frequency domain and then converted to external equivalent current sources, using equations (15) and (43) of *Sun and Egbert* [2012b]. Sources at two periods (14.5 and 3.6 days, in left and right columns, respectively), plotted in Figure 7 (first row), were used for the tests.

Total magnetic fields corresponding to these synthetic sources were generated using the *Sun and Egbert* [2012a] 1-D plus thin sheet forward solver. A fixed 2° × 2° thin conductive sheet at the surface, identical to that used by *Manoj et al.* [2006], with an underlying 1-D conductivity profile (Table 1) slightly modified from *Kuvshinov and Olsen* [2006] were used here and in subsequent inversions of real data. The synthetic surface field data (Figure 8) were sampled at the 220 real observatory locations of Figure 2, and 5% uncorrelated Gaussian noise was added to each of the three field (r, θ, ϕ) components.

Source estimation was then based on minimizing (2) with the same conductivity forward model used to generate the synthetic data, using the source covariance developed in the previous section. Values of the ridge parameter λ in (4) were chosen by the heuristic method of *L* curves [*Hansen*, 1992].

Of course, results depend on the assumed covariance parameters. For these synthetic tests these parameters were chosen empirically; i.e., physically sensible parameters were chosen as a starting point and tuned by hand to obtain lower levels of data misfit and higher visual similarity between the synthetic TIME-GCM sources and the inversion results. This criterion is certainly applicable only to these synthetic tests, where our objective is to verify plausibility and robustness of the covariance model for recovering physically reasonable sources that fit the data. In the real-data inversion presented in section 6, a more sophisticated and exhaustive search for optimal parameter settings is made using a leave-one-out cross validation (LOOCV) scheme [see, e.g., *Hastie et al.*, 2001, chap. 7].

Source inversion results for three sets of covariance parameters, summarized in Table 2, are shown in Figure 7. The three inversions correspond (top to bottom) to decreasing degrees of freedom (DOF) available for fitting the data, controlled primarily by the correlation parameter α. Synthetic and computed magnetic field components are compared for covariance two in Figure 8. Typical normalized root-mean-square (NRMS) misfits for these inversions are all around 1.8 and are generally only very slightly increased for covariances with fewer effective DOF.

From these inversions, we conclude that the quasi-zonal correlated current loop model formulated in the previous section adequately describes ionosphere currents at long periods, as is evident from marked similarities between the TIME-GCM synthetics and the inversion results shown in Figure 7. However, there is room for improvement, as suggested already by our inability to fit to within the noise added to the synthetic data. In particular, sharp gradients in magnetic fields, presumably associated with the equatorial electrojet,
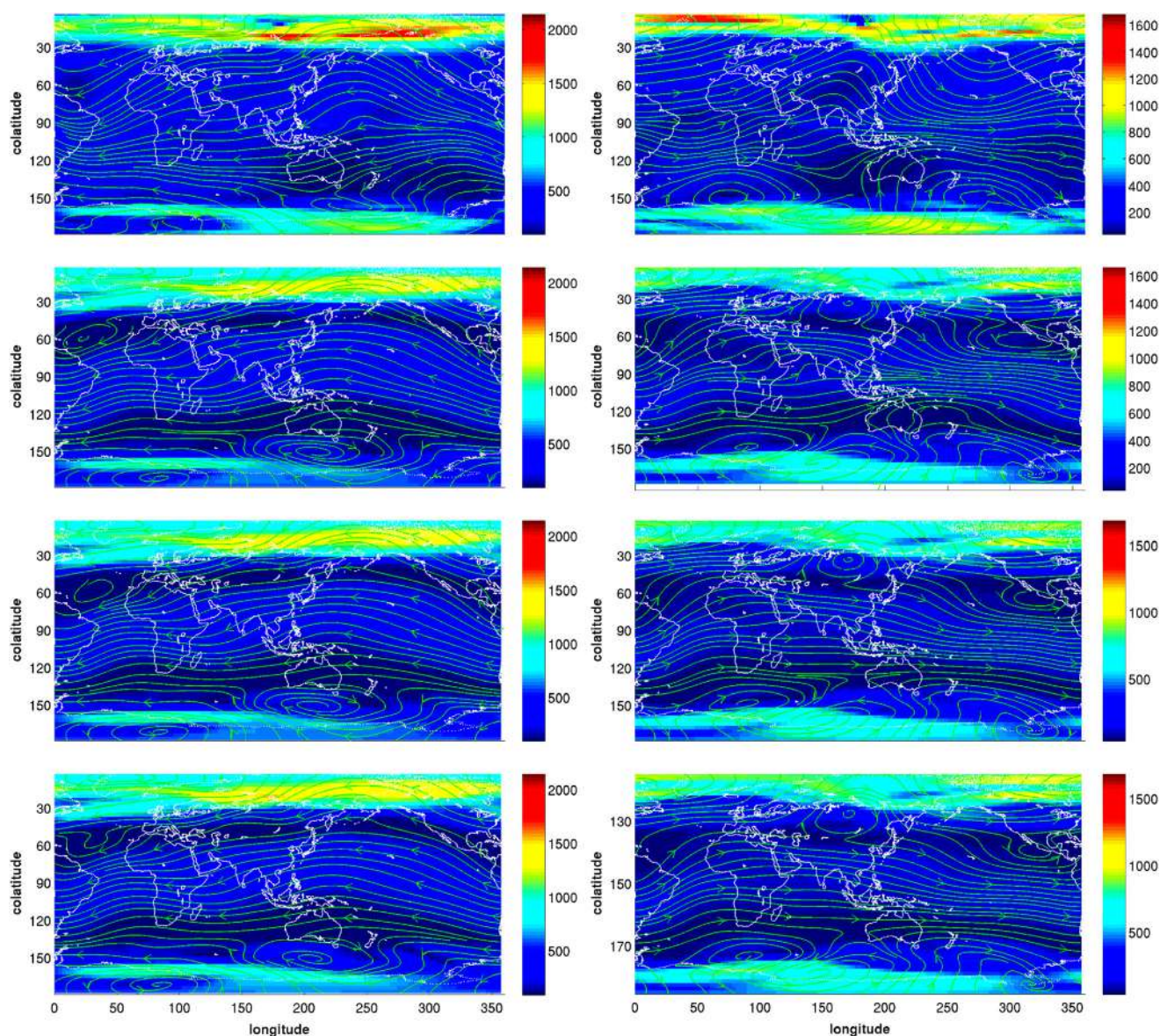
Figure 7. Synthetic source inversion: (first row) real part of the (frequency domain) synthetic source currents derived from the TIME-GCM simulations, at periods (left column) T=14 days and (right column) 3.6 days. (second to fourth rows) Source inversions corresponding to three covariance settings, with decreasing DOF ($\Sigma_L^{(3)}$, $\Sigma_L^{(2)}$, $\Sigma_L^{(1)}$). Plots are in geomagnetic coordinates, with vertical axis representing geomagnetic colatitude. Color gives amplitude, with current sheet streamlines overlain.

are present in the TIME-GCM sources in Figure 8 but are not recovered in the source inversions, regardless of period or covariance parameters tested, and the estimated auroral current systems are somewhat attenuated. The latter is not surprising, given the regularization in the inversion. Also, at some periods there are significant nonzonal components to the synthetic fields at midlatitudes, particularly evident in the ϕ component (Figure 8). However, it is worth bearing in mind that the synthetic sources used for this test differ in some important ways from the sources associated with the real-data modes, the actual focus of our modeling effort. First, the TIME-GCM is strictly an ionospheric model, with no magnetospheric component. Second, we used a rather short run (29 days) to generate the synthetic frequency domain sources, so there is little temporal averaging compared to the actual data modes, which are based on observations over nearly half a century. For example, the TIME-GCM model run is for Northern Hemisphere summer, resulting in a marked north-south asymmetry in auroral zone currents. The nonzonal components evident at midlatitudes might also result from unusual (or seasonal) conditions, and most likely would be reduced with longer averaging.

Table 1. The 1-D Conductivity Profile Used for Forward Modeling and Source Inversions

Depth Range (km)	Conductivity (S/m)
0–40	0.0056
40–250	0.0095
250–410	0.0262
410–670	0.0776
670–900	0.526
900–2400	1.69
2400–2900	10
2900	100

Overall, we consider recovery of the ionospheric source currents quite reasonable, given the relatively sparse spatial sampling of the observatories.

6. Source Inversion Using Real Data

Input data vectors for a range of periods were derived from observatory data as described in section 3, resulting in magnetic field components dominated at midlatitudes by a zonal (geomagnetic) dipole. The estimated magnetic field components are by construction nondimensional, with H_θ of order 1 (near the equator) for all periods. The sources associated with these data vectors are modeled with a two-step procedure, first fitting a P_1^0 source to the data (accounting for induced fields) and then fitting the residual with the regularized inversion, using the source covariance of section 4. In fact, we do not expect the zonal dipole to represent accurately all magnetosphere sources. However, as seen from the ground these complications are indistinguishable from ionospheric sources. We expect that nondipole components of the magnetosphere source at these long periods should still be large scale and quasi-zonal and thus reasonably represented by our ionosphere source model. It is likely that our estimated ionospheric current sheet contains at least some projection from the magnetosphere.

To adjust the free parameters in the source covariance model of section 4 used for fitting the processed observatory data, we start from our experiences with the synthetic data of section 5. Basic parameters such as latitudinal ranges and relative weights, which the synthetic model tests suggest are appropriate to the general ionospheric geometry, were left fixed to values used in section 5. To get some sense of the effects of other parameters on fits achievable for the real data (as defined by NRMS misfit) and on corresponding model structure (assessed visually), we initially tried a large number of source model parameter combinations, with ranges chosen based on the synthetic data results. Based on this initial qualitative evaluation we chose tighter ranges of model parameters (summarized in Table 3) for more systematic determination of optimal covariance parameters for each period. A brief discussion of how variations of covariance parameters in this range impact source complexity and data fit is given in Appendix B.

For the final tuning, we used a leave-one-out cross validation (LOOCV) scheme [see, e.g., *Hastie et al.*, 2001, chap. 7]. The LOOCV score is the NRMS prediction error, estimated by omitting each data point in succession, computing the inverse solution by minimizing (4), and then computing the NRMS of prediction errors for the omitted observations. By doing this for a range of values of λ_s, an optimal value of this ridge parameter can be chosen.

The LOOCV scores may also be used for model selection [e.g., *Arlot and Celisse*, 2010]. The optimal covariance settings for each period were chosen by comparing the optimized LOOCV scores among all parameter combinations tested (see Table 3). In fact, there were generally a range of source covariance models which produced very similar LOOCV scores. We chose the "simpler" model among these, with less tilt (smaller γ_0) and stronger meridional correlation (smaller α). The optimized covariance parameters chosen by this procedure are summarized for all periods in Table 4, with the NRMS misfits for each period given for the full data set, and broken down for high and low latitudes. Corresponding reconstructed source current sheets are plotted in Figure 9 for selected periods. The fitted magnetic field components from these reconstructed sources are shown in Figures 10 and 11, with observations overlain as small colored circles. Note that as our analysis is done in the frequency domain; all quantities are complex; both real and imaginary components are plotted.
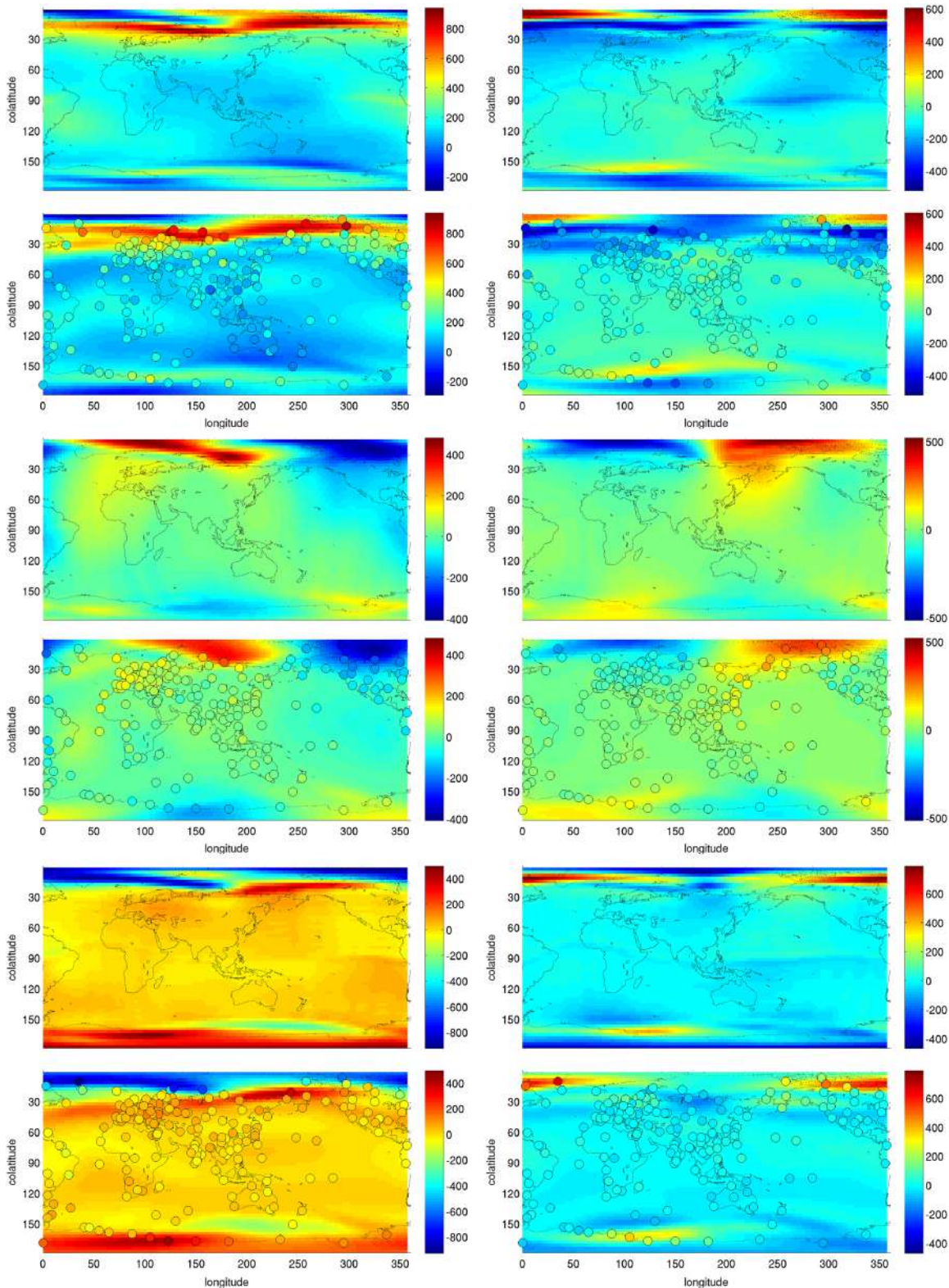
Figure 8. Fit of synthetic data source inversion: (first, third, and fifth rows) real parts of θ, ϕ, and r components of the magnetic fields generated by the TIME-GCM synthetic sources. (left and right columns) For 14 and 3.6 day periods. (second, fourth, and sixth rows) Corresponding fitted field components generated by the inverted sources of Figure 7 with covariance settings $\Sigma_L^{(2)}$. For the fitted component plots data points used for the inversion (i.e., synthetic data sampled at the observatory locations) are overlain, using the same color scale. Note that different color scales are used for different periods to emphasize structure.

Table 2. Covariance Parameters of the Low-Latitude and Northern and Southern Auroral Loops[a]

Loops Collection	Geometric Parameters $(\tilde{\theta}_{min}, \tilde{\theta}_{max}, \gamma_0)$	Incoherence Parameter $\alpha^{(1)}, \alpha^{(2)}, \alpha^{(3)}$	Weight
Low latitude	(−45, 45, 60)	0.05, 0.1, 0.5	0.1
Northern auroral	(55, 85, 120)	10, 20, 30	0.45
Southern auroral	(−85, −55, 120)	10, 20, 30	0.45

[a]The incoherence parameter α takes three values $\alpha^{(1)}$, $\alpha^{(2)}$, and $\alpha^{(3)}$ for each loop collection, corresponding to three loop covariances $\Sigma_L^{(1)}$, $\Sigma_L^{(2)}$, and $\Sigma_L^{(3)}$ of increasing DOF, used for the synthetic source inversions.

Table 4 shows that NRMS misfits increase significantly at shorter periods, especially below 4.6 days, and especially at lower latitudes. This probably reflects several factors. First, error bars are much tighter at short periods (because of the larger number of degrees of freedom in estimates) and at lower latitudes. Sources are more complex at high latitudes and probably require multiple spatial modes to adequately characterize variations in source geometry. This extra variability is treated as noise in our analysis, using a single mode.

These unmodeled source variations contribute to uncertainty in the high-latitude components of the single spatial mode we have estimated for each period. Indeed, Figure 10 suggests that this error scaling is an important factor in the short-period increase in NRMS: fits to the actual data (overlain as small colored circles on the field component images) reveal large-scale coherent patterns that appear reasonably well fit at short periods, while at longer periods (where NRMS is smaller) the data often have a noisier appearance. Some of the misfit also probably results from effects of 3-D conductivity variations that are not accounted for by the simple thin sheet model used, which is based primarily on the ocean-continent conductivity contrast, but ignores other heterogeneity that is certainly present. These effects are likely to be more significant at shorter periods, both due to possibly enhanced heterogeneity at shallower depths, and the impact of normalization by standard errors of the field component estimates. However, the steep increase in NRMS just as periods drop below 5 days is difficult to reconcile with these first two explanations and suggests that shortcomings in our source model at the shortest periods may also be a factor. Indeed, our quasi-zonal current loop model is likely best suited to longer periods, where the averaging effect of Earth's rotation leads to stronger "zonalization" of the effective ionosphere sources. The greater nonzonal complexity, although present in the inversion results for the shortest periods, is likely more difficult to capture with our model.

7. Conductivity Inversion

7.1. Method

In this section we consider inversion for 3-D Earth conductivity with source currents taken from the source inversion step. This is accomplished by minimizing the penalty functional (5), using an extension of the 3-D global electromagnetic (EM) inversion code described in *Kelbert et al.* [2008].

The 3-D forward solver $\bar{\mathbf{G}}_{3D}(\bar{\sigma})$ for the inversion uses the spherical staggered-grid finite difference method implemented by *Uyeshima and Schultz* [2000] to solve the vector Helmholtz equation for the magnetic field **H**, assuming harmonic time dependence $e^{i\omega t}$,

$$\nabla \times (\rho \nabla \times \mathbf{H}) + i\omega\mu_0\mathbf{H} = 0. \tag{13}$$

Here ρ is the electrical resistivity (inverse of conductivity), ω is angular frequency, and μ_0 is the vacuum magnetic permeability. The computational domain includes resistive air layers above the conductive Earth, which

Table 3. Covariance Parameters of the Low-Latitude and Auroral Current Systems Used for the Real-Data Inversion[a]

Loops Collection	$\tilde{\theta}_{min}$	$\tilde{\theta}_{max}$	γ_0	α	Weight
Low latitude	−45	45	{15,30,45,60,75}	{0.1,0.5,1,2,5,10,15,20,25,30}	0.1
Auroral	55	85	{60,90,120,150}	{5,10,15,20,25}	0.45

[a]Identical parameters are used for northern and southern auroral zones. Latitude range parameters $\tilde{\theta}_{min}$ and $\tilde{\theta}_{max}$, as well as weights, were fixed at the synthetic test values, given in Table 2. All combinations of the listed tilt and incoherence parameters were tested, resulting in a total of $4 \times 5 \times 5 \times 10 = 1000$ covariance settings for each period, among which the optimal ones were selected by minimizing LOOCV scores.

Table 4. Optimal Covariance Parameter Settings, as Determined by Minimal LOOCV Score Procedure Described in Text, Sampling Parameter Ranges Given in Table 3[a]

Period (days)	$\gamma_0^{(l)}$	$\gamma_0^{(h)}$	$\alpha^{(l)}$	$\alpha^{(h)}$	NRMS	NRMS$^{(l)}$	NRMS$^{(h)}$	LOOCV Score
1.2	45	90	5	5	3.5	4.2	2.5	4.6
1.6	45	90	1	5	4.6	5.7	2.8	5.4
2.1	45	90	2	5	3.9	4.8	2.7	4.9
2.9	45	90	2	5	4.0	4.8	2.7	5.0
4.6	45	90	2	5	3.9	4.7	2.7	4.9
5.8	45	90	2	5	2.4	2.9	1.7	3.0
8	45	90	2	5	2.4	2.8	1.9	2.9
12	45	90	2	5	2.0	2.3	1.7	2.4
18	45	90	5	10	1.8	1.8	1.6	2.3
26	45	90	5	15	1.5	1.6	1.3	1.8
37	45	90	5	25	1.3	1.3	1.2	1.5
57	45	90	5	25	1.1	1.1	1.0	1.2
102	45	90	5	5	1.1	1.1	1.0	1.2

[a]Corresponding NRMS values are given for all data, and for low and high latitude subsets. The superscripts $^{(l)}$ and $^{(h)}$ refer to low-latitude and high-latitude (auroral) parameter and NRMS values.

extends to the core-mantle boundary where homogeneous boundary conditions are specified. In the original code tangential magnetic fields are specified on the upper boundary to define external source terms in the magnetosphere. The resulting linear equations are solved iteratively using a stabilized biconjugate gradient method, with divergence correction applied periodically to eliminate spurious solutions of the curl-curl equation (13). The forward code is used in a nonlinear conjugate gradients (NLCG) scheme to minimize (5), with the Tikhonov regularization parameter λ_m varied through an automatic cooling scheme. Further details on the inversion can be found in *Kelbert et al.* [2008].

Some extensions to the published scheme are required for this study. Most critically, a secondary field formulation has been introduced to allow for the spatially complex ionospheric sources used here, to improve accuracy, and to achieve better compatibility with the 1-D + thin sheet code used in the source inversion. Specifically, we assume a 1-D background resistivity ρ, and 3-D anomaly $\delta\rho$, with the magnetic field solution divided into corresponding primary (**H**) and secondary (δ**H**) components. Then, in the usual way [e.g., *Alumbaugh et al.*, 1996], the secondary magnetic field satisfies the Helmholtz equation with modified source

$$\nabla \times (\rho + \delta\rho)(\nabla \times \delta\mathbf{H}) + i\omega\mu_0\delta\mathbf{H} = -\nabla \times \delta\rho(\nabla \times \mathbf{H}), \tag{14}$$

and homogeneous boundary conditions. The primary magnetic field **H** is computed for a spherical layered Earth (with resistivity ρ) as in *Sun and Egbert* [2012a]. This is used to compute the right-hand side (RHS) forcing for (14), which is then solved with the spherical 3-D finite difference code. Note that the RHS is nonzero only inside the Earth, so the primary field solution is not required in the air layers.

We also modified the inversion code to allow direct fitting of the three complex magnetic field components (rather than C responses that were previously employed with the P_1^0 source assumption), and we experimented with different conductivity parameterizations. The results shown below have been obtained with a fixed 2° × 2° thin conductive sheet at the surface (based on *Manoj et al.* [2006], consistent with that used for the source inversion), and a crustal layer (12–40 km depths) parameterized as arctan(σ) to allow bounds on conductivity in this layer. Deeper mantle structure is parameterized as in *Kelbert et al.* [2009] as $\log_{10}(\sigma)$ expanded in spherical harmonics. As discussed below, relatively fine resolution (degree 30 and higher) is required to adequately fit the data set considered here. Finally, the modified forward code has been included into the Modular System for Electromagnetic Induction [*Egbert and Kelbert*, 2012; *Kelbert et al.*, 2014] allowing use of parallelized inverse solvers.

7.2. Synthetic Test of the New Conductivity Inversion Technique
To test our new conductivity inversion methodology, we created semirealistic synthetic data sets and inverted these to recover the conductivity structure. We present results of one of these exercises here.
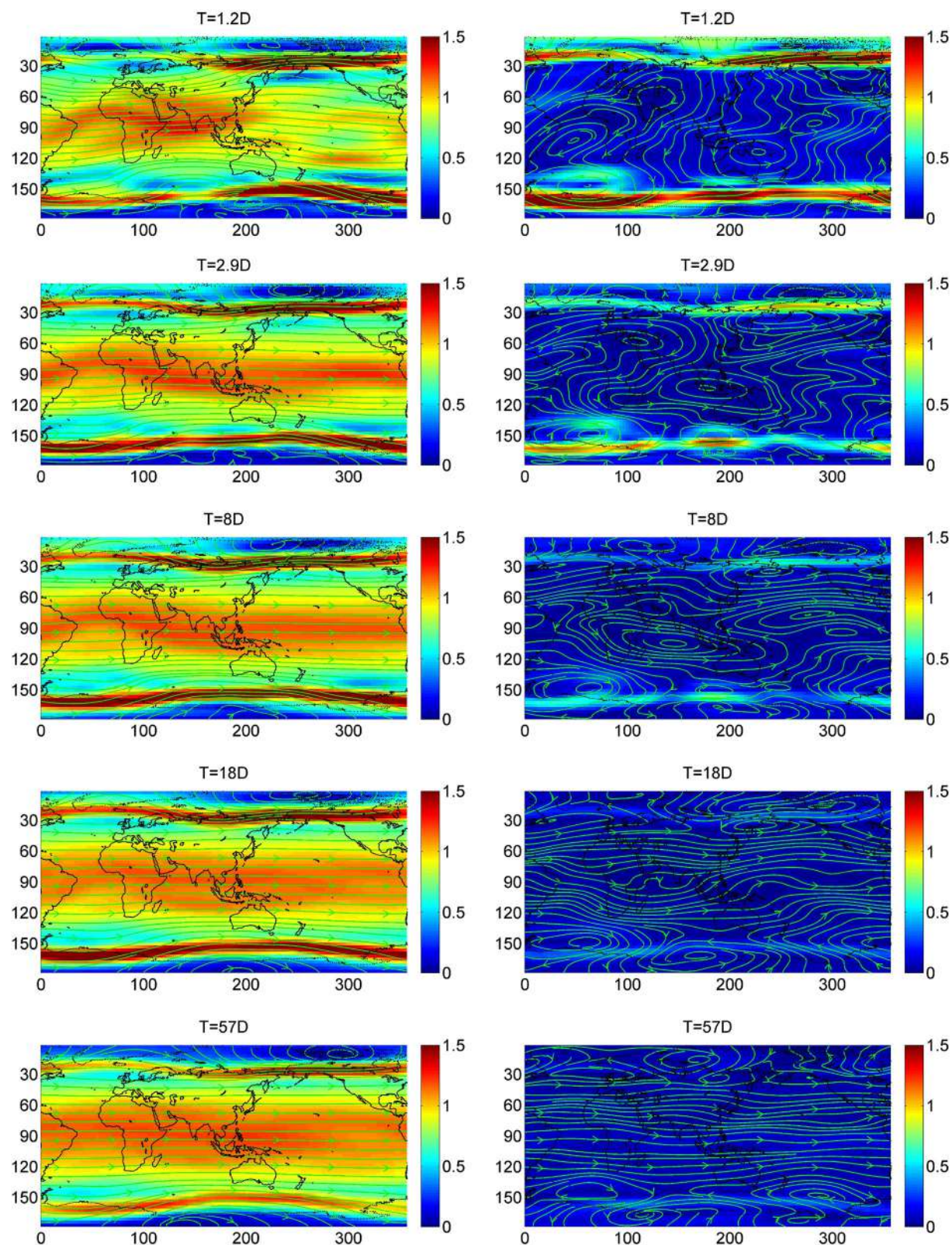
Figure 9. (left column) Real and (right column) imaginary parts of ionospheric source current sheets for a subset of periods, plotted as in Figure 7. Covariance parameters used for the inversions are given in Table 4. All plots are in geomagnetic dipole coordinates.
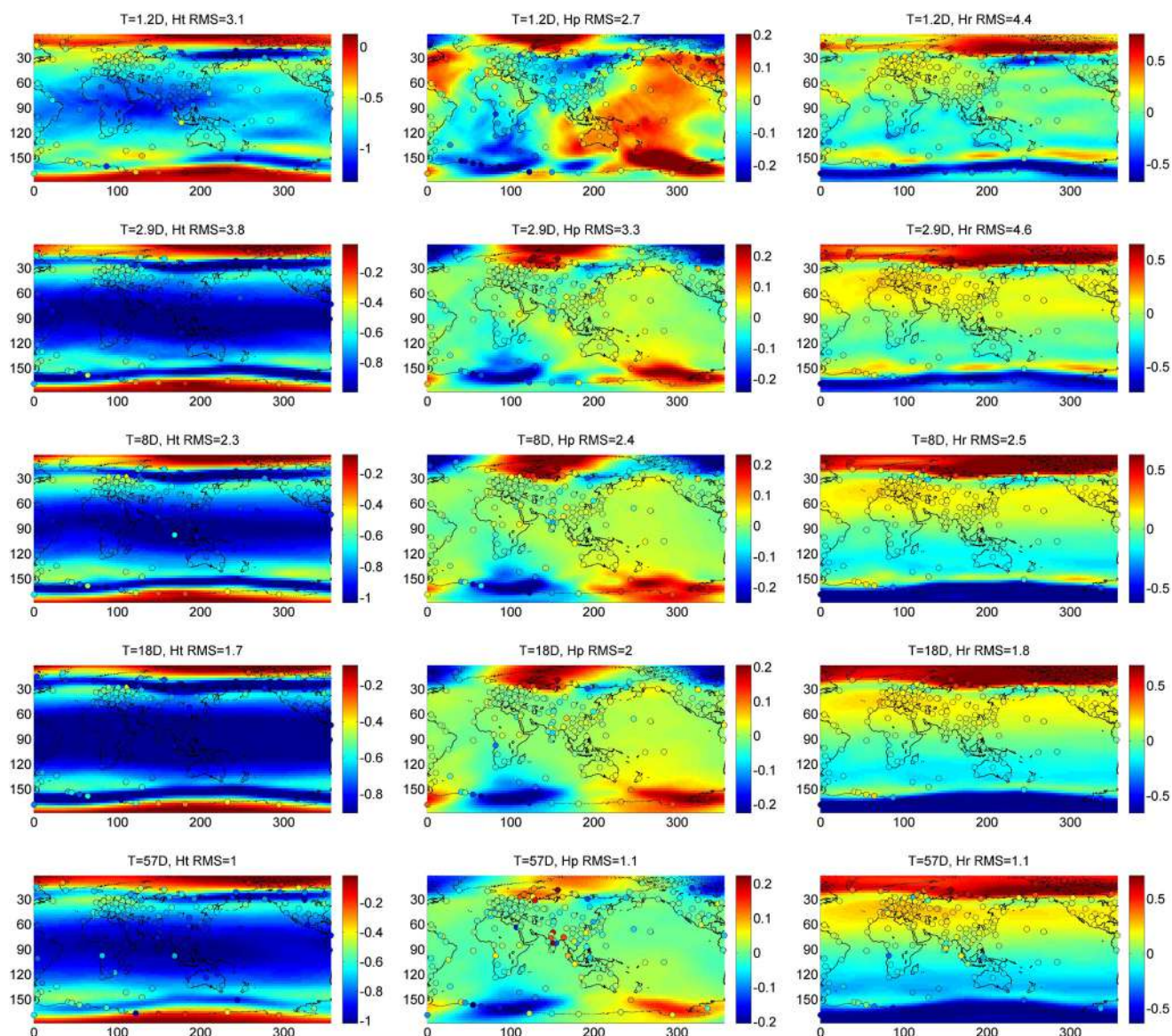
Figure 10. Real parts of fitted magnetic field components from reconstructed sources at periods 1.2, 2.9, 8, 18, and 57 days, from top to bottom. All plots are in geomagnetic dipole coordinates, with (left column) the radial component and (middle and right columns) the geomagnetic east and north components. Data components used for deriving the source model are plotted as filled circles at the observatory locations, using the same color scales used for the field components.

Kelbert et al. [2009] proposed that water introduced in subduction zones could be a major cause for conductive anomalies imaged at depth. We model this scenario with laterally homogeneous mantle with fine-scale inhomogeneities in the upper mantle spatially associated with the subduction zones. The background model was chosen as the 1-D average of a preliminary conductivity inversion of real data, overlain by a laterally heterogeneous thin surface layer representing the ocean-continent contrast [*Manoj et al.*, 2006]. Enhanced subduction zone conductivity in the upper mantle was based on the depth-dependent water flux model of *van Keken et al.* [2011], heuristically scaled to produce representative (but probably only qualitatively realistic) subduction zone conductivity anomalies. For this test the transition zone and lower mantle were laterally homogeneous (Figure 12, left column).

This subduction zone conductivity model was first used to closely imitate the global conductivity inversion reported in *Kelbert et al.* [2009], with synthetic observations closely mimicking the actual data used in this study (59 midlatitude observatories, at 8 periods in the range of 5–100 days). We used the estimated nonzonal source derived from this study (section 6) to generate the synthetic magnetic field data and added realistic
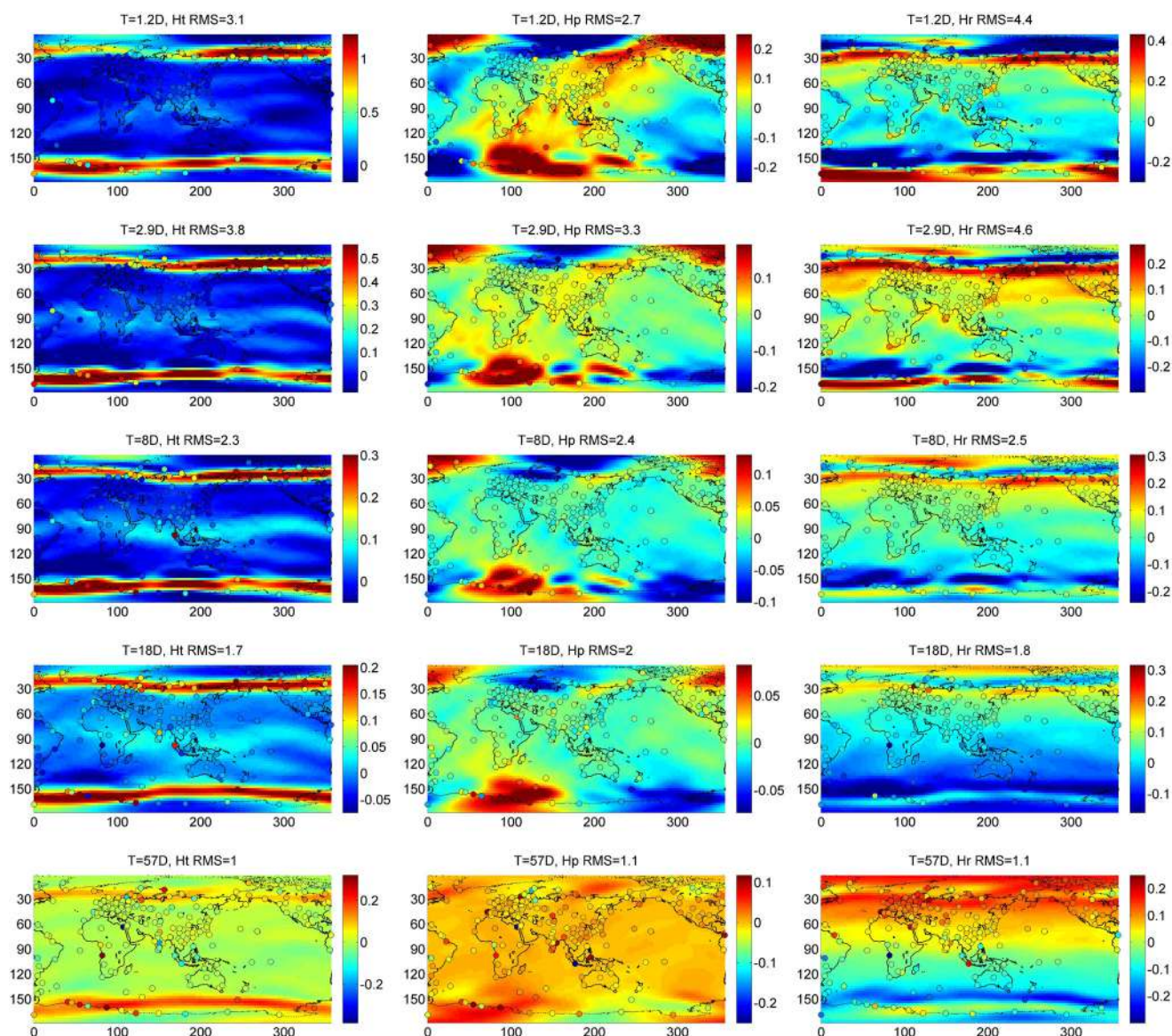
Figure 11. As in Figure 10, but for imaginary components of reconstructed sources, and fitted data (overlain filled circles). As for the real parts periods are, from top to bottom, 1.2, 2.9, 8, 18, and 57 days.

levels of noise (based on error bars of the real data set). We then imitated the auroral correction procedure used by *Kelbert et al.* [2009] to try to reduce auroral source influences on the data. Finally, we inverted the synthetic data set, assuming a purely P_1^0 source and using a model parameterization of spherical harmonic degree and order 9, both consistent with *Kelbert et al.* [2009]. Modeling for this inversion used a $2 \times 2°$ grid (finer than that used by *Kelbert et al.* [2009]), to allow for a more direct comparison with results obtained with the new approach.

With this setup, the inversion recovers broad subduction zone anomalies in the upper mantle. However, even higher-amplitude anomalies appear deep into the transition zone, where the synthetic model was homogeneous (Figure 12, middle column). These results clearly demonstrate how overly simplistic source assumptions (possibly in conjunction with limited data bandwidth) can cause artifacts at depth. No structure is recovered by the inversion at 40–250 km depths. With the shortest period at 5 days there is little sensitivity to uppermost mantle structure.

We next test the inversion using the correct complex source, with synthetic model outputs sampled at the 210 observatory locations and at the 1.2–100 days period range available from our new data analysis. For this
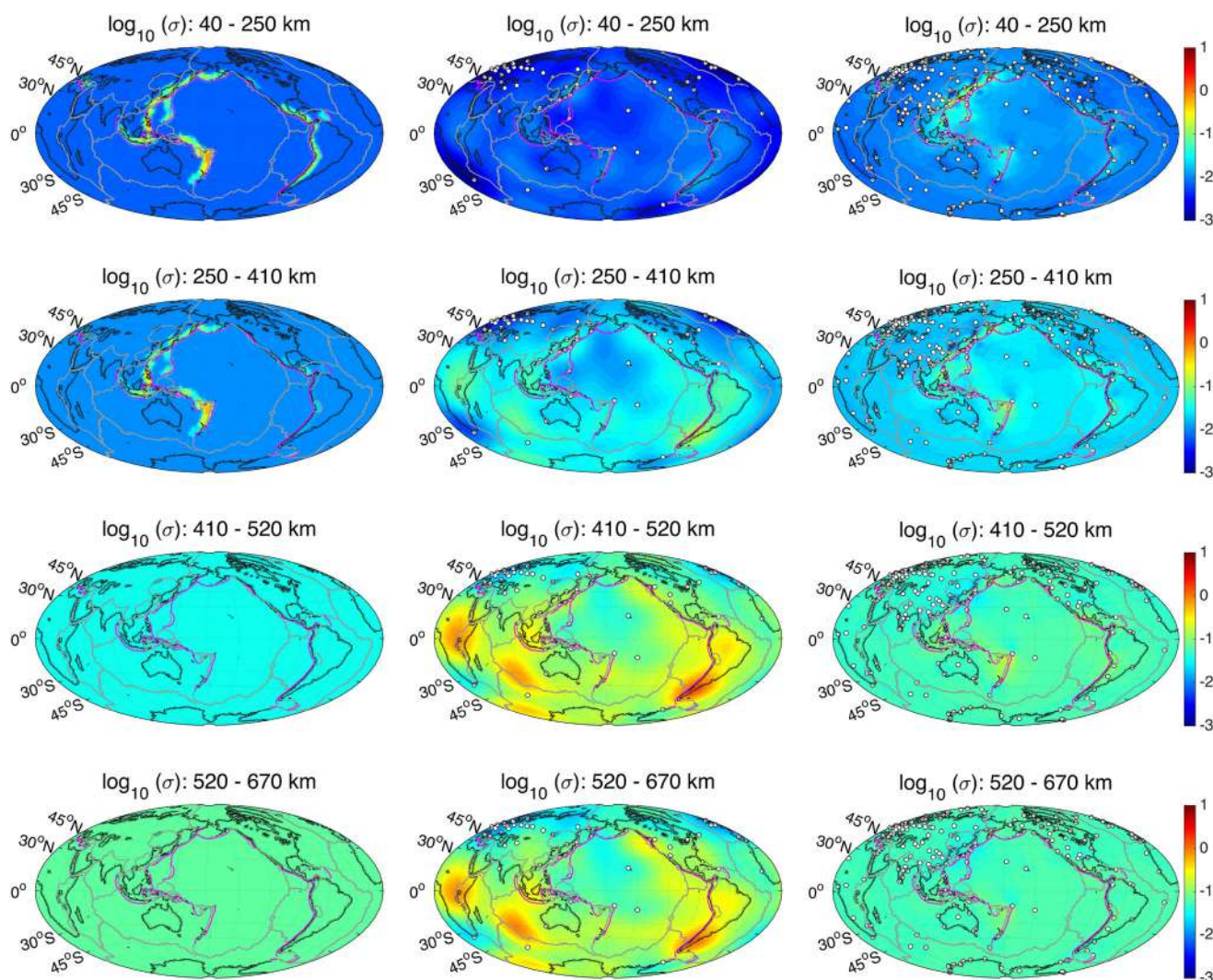
Figure 12. Synthetic conductivity inversion setup and results based on the assumption that all electrical conductivity variations in the mantle are caused by the slab releasing water in the upper mantle during subduction. (left column) A synthetic conductivity model based on *van Keken et al.* [2011]. (middle column) Degree and order 9 inversion at the observatory locations and period subset appropriate for comparison with the *Kelbert et al.* [2009] paper, assuming a grossly simplified P_1^0 source. (right column) Degree and order 40 inversion appropriate for comparison with the real-data results obtained in this work.

test we used a degree and order 40 electrical conductivity parametrization in the mantle. Now, we find a reasonably accurate recovery of the subduction-related anomalies (Figure 12, right column), albeit somewhat smoothed and with reduced amplitude. There remains some leakage into the deeper homogeneous layers, but compared to the first test, this is quite subdued, and there are no significant deep artifacts. This test clearly demonstrates that our 3-D conductivity inversion allowing for general sources performs reasonably, provided we have sufficiently precise knowledge of the external source fields. In section 5 we showed we could reasonably recover sources with known conductivity. We have not yet fully tested the more realistic and challenging case where both source and 3-D conductivity are unknown, which would be best approached with a true simultaneous inversion scheme.

7.3. Results

For completeness we present results of applying the 3-D electrical conductivity inversion to the real data, with the preferred minimal LOOCV source estimate (see Figure 9 and Table 4). The starting total NRMS over all periods for this source and a 1-D Earth with thin sheet is 2.63. The inversion required 46 NLCG iterations to achieve NRMS = 1.71. The resulting 3-D mantle conductivity model is shown in Figure 13 (right column) along with results from *Kelbert et al.* [2009] (left column) for comparison.
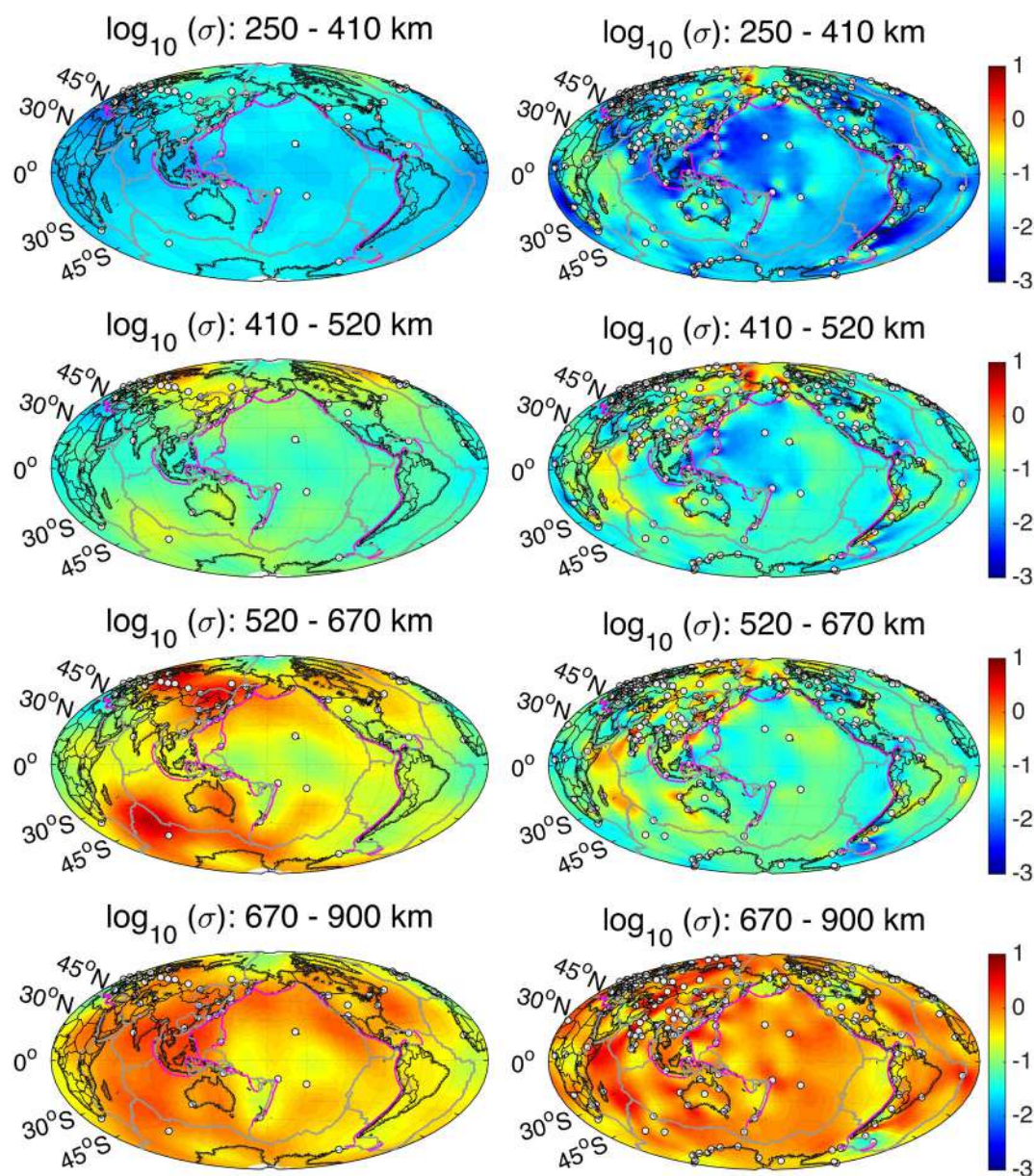
Figure 13. (left column) Electrical conductivity inversion results presented earlier in *Kelbert et al.* [2009]. (right column) Electrical conductivity inversion results obtained with estimated ionospheric source currents obtained with the covariance parameters given in Table 4 (see Figure 7). Plotted are $\log_{10}(\sigma)$, where σ is electrical conductivity in S/m. See text for discussion of this comparison.

The present study represents an advance over the earlier work in several important respects. First, we have allowed for significantly more realistic external current systems and thus expect source contamination to be reduced (see section 7.2). Second, we make use of a considerably larger and higher-quality data set, fitting all three magnetic field components from 210 sites, extending to essentially all latitudes and covering the period range 1.2–100 days. *Kelbert et al.* [2009] fit C responses in the period range 5–100 days, from 59 observatories restricted to latitudes below 55°. In addition to the improved data coverage (evident in Figure 13), data quality is also substantially improved at many of the common sites, with smoother, more physically consistent estimates and smaller error bars. To adequately fit this extended and improved data set requires significantly higher resolution, both in terms of the model parameterization (spherical harmonic degree and order 40 versus 9) and numerical model grid (2° × 2° versus 10° × 10°). Consistent with the resolution analysis of *Kelbert et al.* [2008], and the synthetic results of section 7.2, including shorter-period data results in significantly more structure in the upper mantle, and better depth resolution. The resulting electrical

conductivity models exhibit short-wavelength structures extending from the lithosphere to approximately 1600 km depth. These features appear required to fit the data to the level achieved but should be interpreted with caution. It is quite likely that small-scale, large-amplitude, and possibly anisotropic, conductivity variations are present in the upper mantle. However, even in our new data set sites are sparsely distributed over much of the Earth, and the imaged structures may be spatially aliased or result from the inversions attempt to represent effects of anisotropy or subgrid-scale structure. Furthermore, we have not explored trade-offs between source complexity and conductive heterogeneity systematically enough to rule out source-based artifacts in the conductivity images. A detailed analysis of such trade-offs, as well as resolution analysis, hypothesis testing, and geodynamic interpretation of the conductivity results are beyond the scope of this paper and will be presented in subsequent publications.

With these caveats, we suggest that the principal conclusion of *Kelbert et al.* [2009] that electrical conductivity is elevated in the transition zone around the Pacific margin, most likely due to water carried to great depth by old subducting plates, is supported by the new results. In particular, in addition to the high conductivities seen in both inverse solutions beneath eastern Asia, the new solution now shows high conductivities in the Andean subduction zone, where (in contrast to the earlier study) there are at least a few sites. There are, however, many differences in detail between the mantle conductivity models. To some extent this reflects the fact that much finer-scale structures are required to fit the new data; when the new inversion is parameterized at comparable resolution (spherical harmonic degree 9), consistency with *Kelbert et al.* [2009] becomes even more evident.

8. Discussion and Conclusions

Long-period global EM induction studies of deep mantle conductivity are by necessity based almost exclusively on MV methods (using magnetic fields only) and thus require significant knowledge of external source spatial structure. The classical approach has been to limit interpreted data to events, period ranges, and latitudes where highly simplified source models may plausibly be assumed. Limitations of this approach become acute as one tries to resolve lateral variations in mantle conductivity through 3-D inversion—an ambitious objective that will require interpretation of all available data. To overcome the challenge of uncertain and complex external sources, and to make better use of all available data, we have developed methods for joint modeling of source structure and 3-D conductivity. Here we describe initial application of these methods to long period ($T \geq 1.2$ days) geomagnetic variation data from the global array of observatories. Although the basic idea of joint source/conductivity inversion has been presented previously [*Fainberg et al.*, 1990a; *Singer et al.*, 1993; *Koch and Kuvshinov*, 2013], our scheme involves several novel features, including preliminary data reduction through a PCA approach, and regularization of the external source inversion through a physically based parameter covariance.

The initial frequency domain data reduction step, which extracts the dominant spatially coherent source components from the raw data, is analogous to estimation of transfer functions, but without the need for explicit assumptions about external sources. As with transfer functions, our approach allows data from different eras to be merged; our study includes data from 210 observatories, some only recently installed, and some long inactive. Variants of the simple scheme employed here, based on robust PCA allowing for missing data [*Smirnov and Egbert*, 2012], can be applied to estimate a broader set of data modes, e.g., to capture the spectrum of coherent daily magnetic field variations, which will certainly require multiple modes at each period. On the other hand, the source covariance developed here is rather specific to the long periods considered; application to other period ranges (e.g., daily variations) would require significant modifications, to capture relevant source properties. In addition to allowing for large-scale (geomagnetic dipole) fields due to the magnetospheric ring current, the present source covariance allows for quasi-zonal current systems (smoothed by rotation of the Earth), generated as a superposition of tilted zonal (quasi-dipole) loops. Although simplistic compared to actual current systems (e.g., all sources lie on a current sheet of fixed altitude), the covariance adequately accounts for latitudinal variations in amplitudes and spatial correlation lengths (both azimuthal and meridional) in the dominant spatial modes estimated for long-period geomagnetic variations.

The source inversion, in combination with the initial data reduction scheme, allows us to use all three components of the magnetic field response (instead of just local ratios of field components previously used) and to greatly extend period and latitude ranges. For the first time we are thus able to use most of the available long period observatory data in a 3-D conductivity inversion. To this end we have adapted the 3-D inversion of *Kelbert et al.* [2008] to directly fit field components and to allow for complex (and essentially arbitrary)

specified external source structure. As a next step, the source and conductivity inversion steps will be more tightly coupled, at least initially by allowing for fully 3-D conductivity models in the source inversion, and iterating the two inversion steps. Our focus here has been on the individual steps required for such a coupled inversion, with particular focus on developing a model for external sources tailored to long-period quasi-zonal external current systems.

It should be noted that the auroral current systems we have modeled and included as sources in the inversion are mostly rather narrow. At long periods, where skin depths become comparable to source widths, induction in the Earth will be significantly reduced. However, while these auroral sources may be ineffective at probing deep Earth conductivity, they must be accurately modeled (as external field) to use the longer wavelength components to determine Earth conductivity. While one could try and "correct" the data using the estimated small-scale sources and only use larger-scale source for the inversion, using the full range of source scales for the inversion seems the cleanest approach.

Our application to the available long-period observatory data results in a new, but very preliminary, 3-D model of mantle conductivity. Although this model shares some features with previous global results [e.g., *Kelbert et al.*, 2009; *Semenov and Kuvshinov*, 2012], there are also significant differences. Data coverage has been significantly improved, with more than twice as many sites used, and the period range extended close to 1 day. While model results (and the increased amount of data used) suggest improved resolution (both in depth and laterally), there are significant uncertainties that beg further investigation: trade-offs between fitting the data with complexity in source versus conductivity, possible systematic errors in the geomagnetic data, and sensitivity of model features to relaxing data fit. A more detailed analysis of these issues, as well as interpretation of the inversion results, will be presented elsewhere.

Appendix A: A Heuristic Construction of the Proximity Function

The proximity function $O(L_1, L_2)$ in (9) is an essential component in the covariance model described in section 4. It is used to define the degree to which two current loops are correlated. The value of $O(L_1, L_2)$ lies between 0 and 1, where 0 indicates completely uncorrelated loops and 1 indicates complete correlation. No negative correlations are allowed by construction. From an intuitive point of view, loops that are geometrically and geographically close to each other are assumed to be highly correlated, and those that are far from each other are assumed to be uncorrelated. Therefore, $O(L_1, L_2)$ should measure the "inverse distance" between two loops.

In order to define this distance under spherical geometry, we first define an effective distance between the centers of two loops, taking into account both the latitudinal distance $d_l = |\cos\theta_1 - \cos\theta_2|$ and tilting distance $d_t = \sin\gamma_{1,2}$, where $\gamma_{1,2}$ is the angle between the orientation of the loops' centers relative to the center of the Earth. The effective distance is then defined as $d = \sqrt{d_l^2 + d_t^2}$. Given d and the loops' radii, the proximity $O(L_1, L_2)$ is defined as the percentage of overlap between two loops *in the same plane* of given center distance and radii, as is illustrated in Figure A1. It should be emphasized that the design of this function aims to provide a simple and sensible measure of loop proximity and is by no means unique.
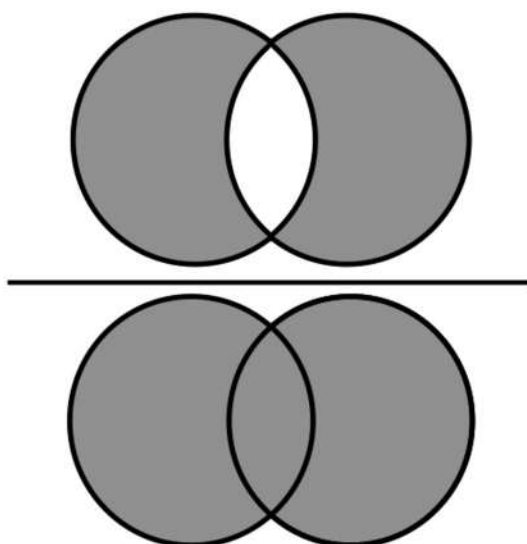

Figure A1. Illustration of current loop "distance," defined as the area of difference normalized by the total area.

Appendix B: Effect of Covariance Parameters on Source Complexity and Data Fit

In this appendix we illustrate how the range of covariance parameters in Table 3 determine realizeable sources, and achievable data misfits. Figure B1 shows data misfits at a period of 8 days, for the LOOCV solution
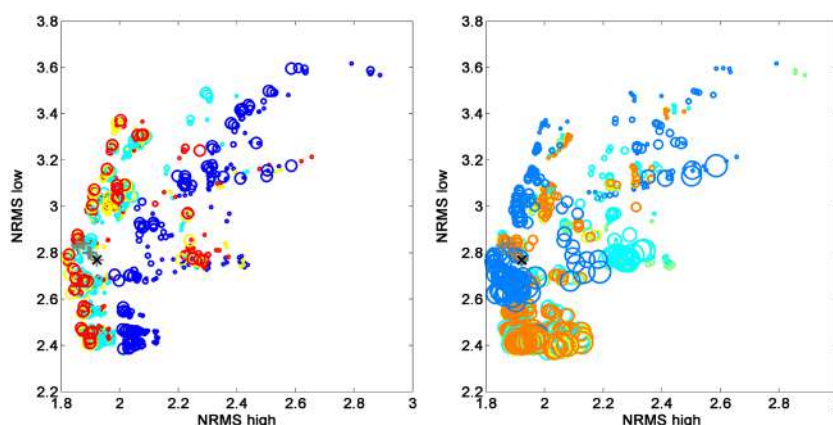
Figure B1. A sample of 1000 covariance parameter settings from Table 3, and their effects on the high-latitude versus low-latitude data misfit, shown at a period of 8 days. Each circle corresponds to a source inversion realization with covariance parameters denoted by color (maximum tilt, γ_0) and size (incoherence, α) values, with warmer colors and larger sizes, in general, corresponding to more source structure. Gray crosses correspond to covariance realizations with the values of LOOCV that are within 0.01 tolerance from the minimum value. The chosen preferred covariance parameter combination is denoted by the black cross. (left) Dependence of NRMS on *high*-latitude covariance parameters $\gamma_0^{(h)}$ and $\alpha^{(h)}$, with $\gamma_0^{(l)}$ and $\alpha^{(l)}$ implicit. (right) Dependence of NRMS on *low*-latitude covariance parameters $\gamma_0^{(l)}$ and $\alpha^{(l)}$, with $\gamma_0^{(h)}$ and $\alpha_{(h)}$ implicit.

found for each configuration of source covariance parameters in Table 3 (1000 combinations in total). In the plot NRMS is subdivided between high latitudes ($NRMS^{(h)}$) and low to middle latitudes ($NRMS^{(l)}$), correspondingly above or below 55° geomagnetic. Warmer colors and bigger circles generally indicate higher-complexity sources and more degrees of freedom for data fitting; see figure caption for details. Dependence on high-latitude covariance parameters is shown in Figure B1 (left), low-latitude parameters in Figure B1 (right).

For example, we see that increasing the maximum allowed tilt at high latitudes, γ_0^h, from 60° to 90° (blue to green in Figure B1, left) provides significant improvement in high-latitude data fit. Further increases in $\gamma_0^{(h)}$ have little impact in reducing misfit. Further, we see that reducing the coherence between auroral current loops (i.e., increasing $\alpha^{(h)}$) does not produce a significant overall improvement in $NRMS^{(h)}$. Away from the auroral zones, going from $\gamma_0^{(l)} = 15°$ to $\gamma_0^{(l)} = 30°$ (blue to green transition in Figure B1, right) also significantly decreases $NRMS^{(l)}$; further, increases in low-latitude tilt have less of an effect but are still significant. In fact, we see that unless some moderate low-latitude tilt is allowed, $NRMS^{(l)}$ cannot be improved over the value of approximately 2.6. The value of $\alpha^{(l)}$ (incoherence; denoted by size) also plays an important role at low to middle latitudes, with all of the best fitting solutions clustered together between 2.4 and 2.8 $NRMS^{(l)}$ with primarily $\alpha^{(l)} \geq 2$ (large circles).

We also note a smaller cluster of large blue circles appearing on both sides of the plot and corresponding to poor data fit. This indicates that the data cannot be fit with high values of α only (large sizes equal high incoherence): unless significant tilting is allowed at some latitudes fit is poor.

References

Alumbaugh, D., G. A. Newman, L. Prevost, and J. N. Shadid (1996), Three-dimensional wide band electromagnetic modeling on massively parallel computers, *Radio Sci.*, *33*, 1–23.
Arlot, S., and A. Celisse (2010), A survey of cross-validation procedures for model selection, *Statistics surveys*, *4*, 40–79.
Bahr, K., and J. H. Filloux (1989), Local S_q responses from EMSLAB data, *J. Geophys. Res.*, *95*, 14,195–14,200.
Banks, R. J. (1969), Geomagnetic variations and the electrical conductivity of the upper mantle, *Geophys. J. R. Astron. Soc.*, *17*, 457–487.
Banks, R. J., and J. N. Ainsworth (1992), Global induction and the spatial structure of mid-latitude geomagnetic variations, *Geophys. J. Int.*, *110*, 251–266.
Egbert, G. D. (1989), Multivariate analysis of geomagnetic array data: 2. Random source models, *J. Geophys. Res.*, *94*, 14,249–14,265.
Egbert, G. D. (1997), Robust multiple-station magnetotelluric data processing, *Geophys. J. Int.*, *130*(2), 475–496.
Egbert, G. D. (2002), Processing and interpretation of electromagnetic induction array data, *Surv. Geophys.*, *23*(2–3), 207–249.
Egbert, G. D., and J. R. Booker (1986), Robust estimation of geomagnetic transfer functions, *Geophys. J. R. Astron. Soc.*, *87*(1), 173–194.
Egbert, G. D., and J. R. Booker (1989), Multivariate analysis of geomagnetic array data: 1. The response space, *J. Geophys. Res.*, *94*, 14,227–14,247.
Egbert, G. D., and A. Kelbert (2012), Computational recipes for electromagnetic inverse problems, *Geophys. J. Int.*, *189*, 251–167.

Eisel, M., and G. D. Egbert (2001), On the stability of magnetotelluric transfer function estimates and the reliability of their variances, *Geophys. J. Int.*, *144*, 65–82.

Emmert, J. T., A. D. Richmond, and D. P. Drob (2010), A computationally compact representation of Magnetic-Apex and Quasi-Dipole coordinates with smooth base vectors, *J. Geophys. Res.*, *115*, A08322, doi:10.1029/2010JA015326.

Fainberg, E. B., and B. Zinger (1980), Electromagnetic induction in a nonuniform spherical model of the Earth, *Ann. Geophys.*, *36*, 127–134.

Fainberg, E. B., A. Kuvshinov, L. P. Mishina, and B. S. Singer (1990a), The new approach to global deep sounding, *Pure Appl. Geophys.*, *134*(4), 527–531.

Fainberg, E. B., A. Kuvshinov, and B. S. Singer (1990b), Electromagnetic induction in a spherical Earth with nonuniform oceans and continents in electric contact with the underlying medium: 1. Theory, method and example, *Geophys. J. Int.*, *102*(2), 273–281.

Fainberg, E. B., A. V. Kuvshinov, and B. S. Singer (1990c), Electromagnetic induction in a spherical Earth with non-uniform oceans and continents in electric contact with the underlying medium—II. Bimodal global geomagnetic sounding of the lithosphere, *Geophys. J. Int.*, *102*, 283–286.

Fujii, I., and A. Schultz (2002), The 3D electromagnetic response of the Earth to ring current and auroral oval excitation, *Geophys. J. Int.*, *151*(3), 689–709.

Hansen, P. (1992), Analysis of discrete ill-posed problem by means of the L-curve, *SIAM Rev.*, *34*, 561–580.

Hastie, T., R. Tibshirani, and J. Friedman (2001), *The Elements of Statistical Learning, Springer Ser. in Stat.*, Springer, New York.

Huber, P. J. (1981), *Robust Statistics*, Wiley, New York.

Kelbert, A., G. D. Egbert, and A. Schultz (2008), Non-linear conjugate gradient inversion for global EM induction: Resolution studies, *Geophys. J. Int.*, *173*(2), 365–381, doi:10.1111/j.1365-246X.2008.03717.x.

Kelbert, A., A. Schultz, and G. D. Egbert (2009), Global electromagnetic induction constraints on transition-zone water content variations, *Nature*, *460*(7258), 1003–1006.

Kelbert, A., N. Meqbel, G. D. Egbert, and K. Tandon (2014), ModEM: A modular system for inversion of electromagnetic geophysical data, *Comput. Geosci.*, *66*, 40–53, doi:10.1016/j.cageo.2014.01.010.

Koch, S., and A. Kuvshinov (2013), Global 3-D EM inversion of Sq variations based on simultaneous source and conductivity determination: Concept validation and resolution studies, *Geophys. J. Int.*, *195*, 98–116, doi:10.1093/gji/ggt227.

Koch, S., and A. Kuvshinov (2015), 3-D EM inversion of ground based geomagnetic Sq data. Results from the analysis of the Australian array (AWAGS) data, *Geophys. J. Int.*, *200*, 1284–1296.

Kuvshinov, A., and N. Olsen (2006), A global model of mantle conductivity derived from 5 years of CHAMP, Ørsted, and SAC-C magnetic data, *Geophys. Res. Lett.*, *33*, L18301, doi:10.1029/2006GL027083.

Kuvshinov, A., D. B. Avdeev, and O. Pankratov (1999), Global induction by Sq and Dst sources in the presence of oceans: Bimodal solutions for non-uniform spherical surface shells above radially symmetric earth models in comparison to observations, *Geophys. J. Int.*, *137*(3), 630–650.

Kuvshinov, A. V., N. Olsen, D. B. Avdeev, and O. V. Pankratov (2002), Electromagnetic induction in the oceans and the anomalous behaviour of coastal C-responses for periods up to 20 days, *Geophys. Res. Lett.*, *29*(12), 1595, doi:10.1029/2001GL014409.

Kuvshinov, A. V., C. Manoj, N. Olsen, and T. Sabaka (2007), On induction effects of geomagnetic daily variations from equatorial electrojet and solar quiet sources at low and middle latitudes, *J. Geophys. Res.*, *112*, B10102, doi:10.1029/2007JB004955.

Manoj, C., A. Kuvshinov, S. Maus, and H. Lühr (2006), Ocean circulation generated magnetic signals, *Earth Planets Space*, *58*, 429–437.

Olsen, N. (1998), The electrical conductivity of the mantle beneath Europe derived from C-responses from 3 to 720 Hr, *Geophys. J. Int.*, *133*(2), 298–308.

Olsen, N. (1999), Long-period (30 Days–1 Year) electromagnetic sounding and the electrical conductivity of the lower mantle beneath Europe, *Geophys. J. Int.*, *138*(1), 179–187.

Püthe, C., and A. Kuvshinov (2014), Mapping 3-D mantle electrical conductivity from space: A new 3-D inversion scheme based on analysis of matrix Q-responses, *Geophys. J. Int.*, *197*(2), 768–784.

Püthe, C., A. Kuvshinov, and N. Olsen (2015), Handling complex source structures in global EM induction studies: From C-responses to new arrays of transfer functions, *Geophys. J. Int.*, *201*(1), 318–328.

Qian, L., et al. (2014), The NCAR TIE-GCM: A community model of the coupled thermosphere/ionosphere system, in *Modeling the Ionosphere-Thermosphere System, Geophys. Monogr. Ser.*, edited by J. Huba, R. Schunk, and G. Khazanov, pp. 73–84, John Wiley, Chichester, U. K.

Richmond, A., E. Ridley, and R. Roble (1992), A thermosphere/ionosphere general circulation model with coupled electrodynamics, *Geophys. Res. Lett.*, *19*(6), 601–604.

Richmond, A. D. (1995), Ionospheric electrodynamics using magnetic apex coordinates, *J. Geomagn. Geoelectr.*, *47*, 191–212.

Sabaka, T. J., N. Olsen, and M. E. Purucker (2004), Extending comprehensive models of the Earth's magnetic field with Ørsted and CHAMP data, *Geophys. J. Int.*, *159*(2), 521–547, doi:10.1111/j.1365-246X.2004.02421.x.

Sabaka, T. J., L. Tøffner-Clausen, and N. Olsen (2013), Use of the comprehensive inversion method for Swarm satellite data analysis, *Earth Planets Space*, *65*(11), 1201–1222.

Schmucker, U. (1999a), A spherical harmonic analysis of solar daily variations in the years 1964–1965: Response estimates and source fields for global induction—I. Methods, *Geophys. J. Int.*, *136*(2), 439–454.

Schmucker, U. (1999b), A spherical harmonic analysis of solar daily variations in the years 1964–1965: Response estimates and source fields for global induction—II. Results, *Geophys. J. Int.*, *136*(2), 455–476.

Schultz, A. (1990), On the vertical gradient and associated heterogeneity in mantle electrical-conductivity, *Phys. Earth Planet. Inter.*, *64*(1), 68–86.

Schultz, A., and J. C. Larsen (1987), On the electrical-conductivity of the mid-mantle. 1. Calculation of equivalent scalar magnetotelluric response functions, *Geophys. J. Int.*, *88*(3), 733–761.

Semenov, A., and A. Kuvshinov (2012), Global 3-D imaging of mantle conductivity based on inversion of observatory C-responses—II. Data analysis and results, *Geophys. J. Int.*, *191*, 965–992, doi:10.1111/j.1365-246X.2012.05665.x.

Shimizu, H., T. Koyama, K. Baba, and H. Utada (2009), Three-dimensional geomagnetic response functions for global and semi-global scale induction problems, *Geophys. J. Int.*, *178*(1), 123–144.

Shimizu, H., H. Utada, K. Baba, T. Koyama, M. Obayashi, and Y. Fukao (2010), Three-dimensional imaging of electrical conductivity in the mantle transition zone beneath the North Pacific Ocean by a semi-global induction study, *Phys. Earth Planet. Inter.*, *183*(1–2), 252–269, doi:10.1016/j.pepi.2010.01.010.

Singer, B. S., A. Kuvshinov, L. P. Mishina, and E. B. Fainberg (1993), Global geomagnetic sounding: New methodology and results, *Izv. Phys. Solid Earth*, *29*, 35–43.

Smirnov, M. Y., and G. D. Egbert (2012), Robust principal components analysis of electromagnetic arrays with missing data, *Geophys. J. Int.*, *94*, 1423–1438, doi:10.1111/j.1365-246X.2012.05569.x.

Sun, J., and G. D. Egbert (2012a), A thin-sheet model for global electromagnetic induction, *Geophys. J. Int.*, *189*(1), 343–356, doi:10.1111/j.1365-246X.2012.05383.x.

Sun, J., and G. D. Egbert (2012b), Spherical decomposition of electromagnetic fields generated by quasi-static currents, *GEM - Int. J. Geomath.*, *3*(2), 279–295, doi:10.1007/s13137-012-0039-0.

Utada, H., T. Koyama, H. Shimizu, and A. D. Chave (2003), A semi-global reference model for electrical conductivity in the mid-mantle beneath the North Pacific Region, *Geophys. Res. Lett.*, *30*(4), 1194, doi:10.1029/2002GL016092.

Utada, H., T. Koyama, M. Obayashi, and Y. Fukao (2009), A joint interpretation of electromagnetic and seismic tomography models suggests the mantle transition zone below Europe is dry, *Earth Planet Sci Lett.*, *281*(3–4), 249–257, doi:10.1016/j.epsl.2009.02.027.

Uyeshima, M., and A. Schultz (2000), Geomagnetic induction in a heterogeneous sphere: A new three-dimensional forward solver using a conservative staggered-grid finite difference method, *Geophys. J. Int.*, *140*(3), 636–650.

van Keken, P. E., B. R. Hacker, E. M. Syracuse, and G. A. Abers (2011), Subduction factory: 4. Depth-dependent flux of H_2O from subducting slabs worldwide, *J. Geophys. Res.*, *116*, B01401, doi:10.1029/2010JB007922.